Metallic Nano to Micro Size Particles Embedded in High Dielectric Ferrites for Effective EMI shielding.

By

Somia Munawer

School of Chemical and Materials Engineering

National University of Sciences and Technology

2023

Metallic Nano to Micro Size Particles Embedded in High Dielectric Ferrites for Effective EMI shielding.

Name: Somia Munawer

Reg. No: 00000320233

This thesis is submitted as a partial fulfillment of the requirements for the degree of

MS (Materials and Surface Engineering)

Supervisor Name: Dr. Muhmmad Siyar

School of Chemical and Materials Engineering (SCME)

National University of Sciences and Technology (NUST)
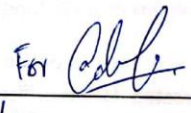
H-12 Islamabad, Pakistan

April 2023

THESIS ACCEPTANCE CERTIFICATE

Certified that final copy of MS thesis written by Ms **Somia Munawar** (Registration No 00000320233), of School of Chemical & Materials Engineering (SCME) has been vetted by undersigned, found complete in all respects as per NUST Statues/Regulations, is free of plagiarism, errors, and mistakes and is accepted as partial fulfillment for award of MS degree. It is further certified that necessary amendments as pointed out by GEC members of the scholar have also been incorporated in the said thesis.

Signature: _____

Name of Supervisor: **Dr Muhammad Siyar**

Date: ___05 - 0 9 - 2023___

Signature (HOD): ___For (signature)___

Date: ___06/09/23___

Signature (Dean/Principal): _____

Date: ___7-9, 2023___

CME)

Form TH-1
(Must be type written)

National University of Sciences & Technology (NUST)
MASTER'S THESIS WORK
Formulation of Guidance and Examination Committee (GEC)

Name: SOMIA MUNAWER

NUST Reg No: MSE-14-~~230233~~ 320233

Department: SCME

Specialization: Materials and Surface Engineering

Credit Hour Completed: **24**

CGPA: **3.00**

Course Work Completed

S/No	Code	Title	Core/Elective	CH	Grade
1	MSE 811	Material Thermodynamics	Core	3	C+
2	MSE 821	Mechanical Behavior of Materials	Core	3	C
3	MSE 831	Manufacturing process	Elective	3	B
4	MSE 812	Phase Transformation of Microstructure	Core	3	B
5	MSE 851	Surface Engineering and Characterization	Core	3	B
6	MSE 862	Electronic and Magnetic Materials	Elective	3	B+
7	MSE 854	Characterization of Materials	Elective	3	A
8	~~NSE 843~~	Advance surface coating — MSE-852	Elective	3	B
9	RM-898	Research methodology	Add	2	Q

Exam B!

Date **5-5-2021**

Student's Signature *Somia*

4/6/21

Thesis Committee

1. Name: **Dr. Muhammad Siyar (Supervisor)**   Signature: _____
   Department: **ME (SCME)**
3. Name: **Dr. Iftikhar Hussain Gul**   Signature: _____
   Department: **ME (SCME)**
4. Name: **Dr. Malik Adeel Umar.**   Signature: _____
   Department: **ME (SCME)**
6. Name: **Dr. Muhmamad Zeeshan Ali**   Signature: _____
   Department: **ME (SCME)**

Date: ~~5-5-2021~~ 28/6/2021

Signature of Head of Department: _____

APPROVAL

Date: ~~5-5-2021~~ 3·6·2021

Dean/Principal

Distribution
1x copy to Exam Branch, Main Office NUST
1x copy to PGP Dte, Main Office NUST
1x copy to Exam branch, respective institute

School of Chemical and Materials Engineering (SCME) Sector H-12, Islamabad

National University of Sciences &Technology (NUST)

FORM TH-4

MASTER'S THESIS WORK

We hereby recommend that the dissertation prepared under our supervision by
Regn No & Name: 00000320233 Somia Munawar

Title: Metallic Nano to Micro Size Particles Embedded in High Dielectric Ferrites for Effective EMI Shielding.

Presented on: 23 Aug 2023   at: 1430 hrs in SCME (Seminar Hall)

Be accepted in partial fulfillment of the requirements for the award of Masters of Science degree in Materials & Surface Engineering.

Guidance & Examination Committee Members

Name: Dr Malik Adeel Umar   Signature:

Name: Dr Zeeshan Ali   Signature:

Name: Dr Iftikhar Hussain Gul   Signature:

Supervisor's Name: Dr Muhammad Siyar   Signature:

                                   Dated: 24 Aug 2023

Head of Department   Dean/Principal
Date 31/08/2023   Date 4.9.2023

School of Chemical &Materials Engineering (SCME)

Dedication

I dedicate this thesis to myself and my friends who have supported me during my degree.

Acknowledgements

First and foremost, I would like to thank Allah Almighty for giving me the strength and opportunity to undertake this research study and to preserve and complete it satisfactorily. Without His blessings, this work would not have been possible.

I wish to express my sincere gratitude to my supervisor, Dr Muhammad Siyar, who has been a tremendous mentor for me. I would like to thank him for his encouragement, enthusiastic supervision, and help during my research and for allowing me to grow as a research scientist. I am also grateful to lab fellows and seniors for their support.

Finally, I would like to thank Sohaib Ahmad my family and friends for their unconditional support and encouragement. To the most important people in my life, my parents, my siblings, this research work could only be completed with your support foremost.

<div align="right">

Somia Munawer

Reg No. 00000320233
</div>

Abstract

In this study, the conventional auto-combustion sol-gel technique was used to synthesize Mg-substituted Zn ferrite with the chemical formula $Mg_xZn_{1-x}Fe_2O_4$ (x = 0.1, 0.25, 0.50, 0.75, and 0.90). The substitutional effect of Mg ion was studied on the structural, dielectric, and electromagnetic interference (EMI) properties of $Mg-ZnFe_2O_4$ ferrite and characterized through X-ray diffraction (XRD), scanning electron microscopy (SEM), infrared spectroscopy (FT-IR), Impedance analyzer (IA) and vector network analysis (VNA). XRD analysis has confirmed the spinel cubic phase pattern with an average crystallite size of 67 to 39 nm. It has been observed that the substitution of Mg significantly affects structural characteristics (such as lattice constant, x-ray density, bulk density, porosity density, etc.) of synthesized Mg- Zn ferrite. Scanning electron microscope examined the surface morphology of the powder. The increasing amount of Mg^{2+} improved the dielectric, and EMI properties of $Mg-ZnFe_2O_4$ ferrite. EMI studies reflect that the absorption properties are better than other samples for the zinc ferrite sample with maximum (0.9) amount of Mg in the sample. Using ball milling, Al incorporation into $Mg_xZn_{1-x}Fe_2O_4$ ((x = 0.1, 0.5, 1%) was achieved successfully. Further using the space charge polarization model of Maxwell-Wagner $Al/Mg_xZn_{1-x}Fe_2O_4$ characteristics like dielectric were explained. The frequency dependent dielectric constant and the dielectric losses were the primary elements of the electrical analysis. Overall EMI shielding results are in well agreement with dielectric properties. EMI absorption performance is enhanced up to SEA= -29.3 dB at 2.9 GHz for $0.5Al/Mg_{0.9}Zn_{0.1}Fe_2O_4$

Table of Contents

List of figures

List of tables

Chapter:1

Introduction

EMI shielding has gained attention and plays a significant role in the modern era since World War-II. With the passage of time, the development of a huge number of electronic and communication devices has been linked to the fast progress in today's modern society. This frequent use of wireless technologies causes electromagnetic radiation pollution and leads to EMI in the surrounding. The performance of electronic appliances is affected by EMI noises which often cause severe failure in these electronic systems. Apart from damaging electronic devices, EMI is equally hazardous to living beings and can cause various diseases like brain tumours, leukemia, rapid heartbeat, increased risks for lung cancer, nausea, DNA strands breakdown, weariness, breast cancer etc [1, 2]. Thus, controlling electromagnetic interferences and developing effective shielding materials which are the interest of the scientific community to reduce the EMI adverse effects. Most of the scientific study has been focused on high-frequency shielding, especially in the region of X-frequency 8.2 to 12.4 GHz but electromagnetic waves are widely used in smart devices such as computers, TVs, radios, mobile phones, etc. in the range of low-frequency 1MHz-3GHz. To protect such equipment, it is essential to understand the EMI shielding effectiveness at low frequencies.

Figure 1 Electromagnetic interference devices

Apart from the very good potential of $Al/Mg_xZn_{1-x}Fe_2O_4$, there are not many reports on its EMI shielding investigation at low frequencies and a detailed analysis of dielectric, and impedance properties is missing. A detailed comprehensive study of its structure-property relationship and the EMI shielding impact is still to be addressed. Here in this research work we tried to examine the behavior of aluminum added Mg-Zn ferrite on EMI shielding where aluminum behave as a scattering site in Mg-Zn ferrite matrix.

1.1 EMI shielding materials.

EMI shielding is a process which includes the utilization of a suitable material to function as a barrier between undesirable signals that may interfere with a device. There exists a multitude of materials that are currently employed for the purpose of shielding against EMI [3]. These materials include, but are not limited to, metallic alloys, metal composites, ceramics, conducting polymer composites, carbon-based materials, composites comprising of polymers like epoxy, and ferrite-based composite [4]. In order to combat EMI, researchers are actively engaged in the development and testing of various materials with selection criteria being based on the application area and surrounding environment, as well as the material's response within a specific frequency range in which it can provide effective shielding [5].

1.2 Materials for shielding based on polymer composite.

Composites derived from the ethylene-vinyl acetate copolymer have been successfully employed for the purpose of EMI shielding. During the production process, it was found that regulating the viscosity of the polymer proved to be a particularly sensitive matter [6]. To develop more effective EMI shielding solutions, researchers have explored the potential of polyvinyl alcohol nanocomposites that incorporate transition metal oxides [5]. However, the use of metal materials in the composite presents a significant drawback in the form of rusting. When applied as a coating, this issue is further compounded by the poor wear resistance properties of the composite material [7].

Conducting polymer composites, namely Polyaniline, Polypyrole, Polythiophene, were utilized for EMI shielding purposes. However, the simultaneous control of the dielectric and magnetic properties of such composites proved to be challenging. These two properties are crucial to the shielding mechanism of the material. A study was conducted on U type Barium hexaferrites (Ba4Co2Fe36O60) in combination with

epoxy composites for their shielding properties, which unfortunately did not exhibit satisfactory performance as a shielding material in the frequency range of 8 GHz to 12 GHz [8].

1.3 Materials for shielding based on metallic alloy.

Metallic alloys have been extensively studied as a material for EMI shielding applications. Nevertheless, the existing literature highlights certain limitations that must be addressed. Several studies have attempted to synthesize alloys for EMI shielding. Kesavapllai et al. have been successful in the synthesis of polyol-derived Nickel and Ni-Fe alloys, which have been found to be appropriate for EMI shielding within the range of 12 GHz to 18 GHz frequencies. However, a challenge with this alloy has been the disturbance of its shielding properties due to the entrapment of moisture during the synthesis process in Polyethylene glycol, which is used as dispersion media [9]. In a separate investigation, Keju et al. have implemented Carbon Nano Tubes into Cu-Ni alloy with the aim of augmenting its microwave absorption characteristics. However, the alloy's porous makeup has acted as a hindrance to its overall robustness and enduringness. Additionally, the utilization of numerous metallic alloys for the purpose of shielding applications has raised substantial apprehension regarding their susceptibility to corrosion [10].

1.4 Materials for shielding based on ferrite.

Ferrite-based substances exhibit significant potential for employment in EMI shielding applications, primarily due to their exceptional electromagnetic wave absorption traits[11]. These materials possess the ability to satisfy a wide range of requisites while simultaneously addressing the obstacles that arise with the synthesis of composite materials that lack ferrites, such as complications and deficiencies in terms of strength and durability. In the pursuit of achieving efficient EMI shielding, J. Liu and colleagues conducted an initial investigation involving the creation of a core-shell composite containing a polyaniline coating on the surface of Barium hexaferrite particles. The results of this experiment were promising, as the composite displayed favourable shielding properties within the X-Band frequency range, or within the gigahertz spectrum. As a result of these findings, ferrites garnered significant attention from researchers as a potential material for EMI shielding applications.

1.5 Substitute ferrite with various cations.

To enhance the magnetic properties for the purpose of EMI shielding applications, numerous transition metals have been employed to replace ferrites, as mentioned in the available literature [12]. Spinel ferrites first appeared by synthesizing zinc Substituted Nickel Ferrites. In the X-band frequencies (8.2–12.4 GHz) rhe Ni-Zn ferrites have been shown better electromagnetic properties which proved them a good choice within this range, but electromagnetic waves are widely used in smart devices i.e., computers, TVs, radios, mobile phones, etc. in the low-frequency range of 1 MHz-3 GHz. To protect such equipment, it is essential to understand the EMI shielding effectiveness at low frequencies. Mixed spinel ferrites, an alternative to spinel ferrites for EMI shielding material in low range frequencies of 1 MHz to 3 GHz were subjected to research and experimentation. It was found that these ferrites demonstrated favourable characteristics thereby making them a viable option for EMI shielding purposes.

EMI can be attributed to the total reflection, absorption, and multiple reflections of electromagnetic energy [13]. The electric conductivity of the material is the primary requirement for reflection shielding whereas magnetic or electric dipole-containing materials are strong contenders for absorption shielding. Multiple reflections occur when electromagnetic waves reflect from different inhomogeneous phase interfaces within the shield material[14]. In existing techniques shielding via an absorption mechanism is the most effective way of interference reduction from a practical perspective. Thus, various kind of ferrites materials with aluminum added filler has been developed to make absorption-based EMI shielding.

1.6 Substitution of Mg-Zn mixed spinel ferrite

Spinel ferrites and aluminum are favourable materials to be used in EMI-absorbing structures in a low-frequency range. For example, magnesium-zinc ferrite ($MgZnFe_2O_4$) is one of the ferrimagnetic spinel ferrites. $MgFe_2O_4$ primarily functions as an inverse spinel ferrite. B sites are occupied by Mg^{2+} ions , whereas Fe^{3+} ions are dispersed between sites A and B with a formula unit $(Fe^{3+})_A [Mg^{2+} Fe^{3+}]_B O_4$. But on the other side, $ZnFe_2O_4$ is a spinel ferrite having the formula unit $(Zn^{2+})_A [Fe_2^{3+}]_B O_4$ where Zn^{2+} ions prefer to occupy A sites [15]. $Mg_{1-x}Zn_xFe_2O_4$ is a mixed spinel ferrite

that has a high degree of permeability, strong chemical stability, high electrical resistivity, low losses, low coercivity, soft magnetic nature, low cost, and high magnetization [16-18]. The stable crystal structure and essentially ionic chemistry of mixed spinel ferrites make them exceptionally stable [19]. It finds its applications in a wide range of fields, including sensors, power transformers, microwave recording media, and radar absorption including sensors, power transformers, microwave recording media, and radar absorption materials devices[13, 20-22]. Aside from being inexpensive, non-polluting, and simple to use, the synthesis of Mg-Zn nanoparticles is achieved via the sol-gel self-combustion and simply aluminum nanoparticles added in Mg-Zn ferrite through ball milling. Among these approaches, Ball milling and sol-gel method which include a self-combustion reaction is the most favourable due to its easy process, low temperature, less time consuming, and economical with highest possible yield and homogenization [23].

1.7 Research objectives

The present study is aimed at achieving the subsequent goals:

- Mg substituting Zn ferrite nanoparticles has been synthesized by using the fast and effective sol-gel combustion method.
- Characterization of the synthesize materials through X-ray diffraction (XRD), scanning Electron microscopy (SEM), infrared spectroscopy (FT-IR), Impedance analyser (IA) and vector network analysis (VNA), LCR meter.
- To enhance the dielectric characteristics and Emi shielding of incorporation of Al in mixed spinel ferrite and

Chapter:2

Literature Review

2.1 Magnetization

A material's ability to respond to an applied magnetic field from its surroundings is referred as magnetism. The alteration of the orientation and alignment of the material's dipoles is brought about by this interaction with the external magnetic field which depends on the material's types. Thus, magnetic materials are classified on the basis of relative orientation and alignment of associated magnetic dipoles. The various types of magnetic materials are examined in detail below.

2.1.1 Diamagnetism

When a material is subjected to a magnetic field applied externally the phenomenon observed as a result of the alteration in the orbital motion of an electron is referred as diamagnetism. This phenomenon arises due to The applide external magnetic field exerts a force of magnetism $F = q(V \times B)$ on the revolving electron in the form of which modifies the centripetal force acting on the electron shows in Figure (2). Consequently, the electron either accelerates or decelerates in its orbital motion. This change in the electron's speed results in the adjustment of the magnetic moment of the orbital, which now opposes the direction of the external magnetic field [24].
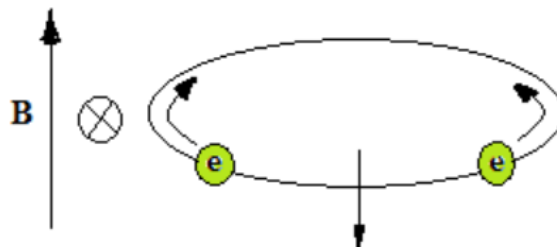
Figure 2 Magnetic field due to movement of electrons [24]

All substances possess inherent diamagnetic properties and those with fully occupied electron shells don't have a net magnetic spin dipole and are classified as pure diamagnetic. Nevertheless, substances with unfilled electron shells exhibit various types of magnetism that surpass diamagnetic effects. Negative magnetic susceptibility is exhibited by diamagnetic materials in by application of a magnetic field owing to the orientation of the produced magnetic moment following being placed into the field. Bismuth, Gold, Silver, and Copper are among the diamagnetic materials that have been identified as exhibiting an intrinsic property of repelling magnetic field.

2.1.2 Paramagnetism

Paramagnetism is a phenomenon that is observable in materials that possess a magnetic dipole moment that is permanent like atoms or ions with unoccupied electron orbits [24]. By application of magnetic field on these types of materials, they get attracted. The individual atoms in such materials in the absence of external filed have a permanent dipole. In a state of pure paramagnetism, these atomic dipoles are not interactive and are randomly oriented resulting in a net moment of zero as shown in Figure (3). When dipole s interacts with each other they have the ability to align or anti-align which can result in either ferromagnetic or antiferromagnetic properties. Furthermore, it is feasible to witness the manifestation of paramagnetic properties in ferromagnetic substances when their temperature surpasses the Curie temperature and in antiferromagnetic materials when their temperature exceeds the Néel temperature.
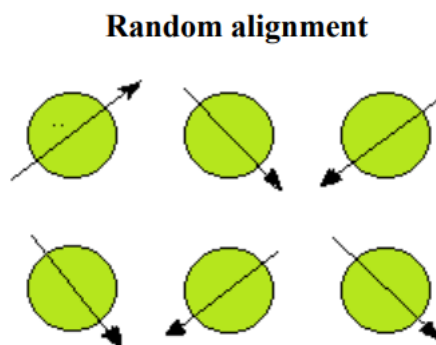
Figure 3 Schematic of Paramagnetism [24]

These substances exhibit magnetism when exposed to a magnetic field however, their magnetic alignment is easily disturbed by thermal agitation upon removal of the field. These materials possess a limited and constructive magnetic susceptibility towards an exogenous magnetic field. Certain materials exhibit paramagnetic properties among which are Titanium, Chromium, and Oxygen[24].

2.1.3 Ferromagnetism

Materials capable of exhibiting spontaneous magnetization characterized by a net magnetic moment without the presence of an applied magnetic field are ferromagnetism. The phenomenon of parallel alignment of atomic magnetic moments is exclusively witnessed in materials having a lattice-like atomic arrangement as depicted in Figure (4). Ferromagnetic elements such as Fe, Co and Ni, listed in the periodic table, exhibit high and positive magnetic susceptibility as a result of externally applied magnetic field at or above room temperature as shown in Figure (4). A distinct property of magnetic materials is being highly responsive to applied fields and capable of preserving their magnetic characteristics even after the external field is no longer present.

Parallel alignment
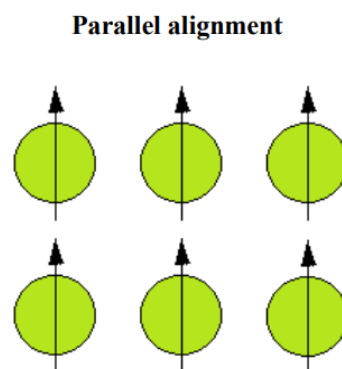
Figure 4 Material exhibiting ferromagnetism[24].

When ferromagnetic materials are exposed to thermal energy their atomic magnetic moment alignment decreases resulting in paramagnetism. This phenomenon is characterized by the Curie temperature which denotes the temperature at which this transition occurs. The transition temperature is 770 C for Fe, 358 C for Ni, and 1131 C for Co. The Curie-Weiss law governs the magnetic susceptibility above Tc. Ferromagnetic materials such as Aluminum, Cobalt, and Iron are among the specimens that demonstrate this particular phenomenon.

2.1.4 Antiferromagnetic

Anti-ferromagnetism is a physical phenomenon characterized by the alignment of two dipoles in opposite orientations, as depicted in Figure (5). The magnetic moment of the whole material is null due to having equal magnitude of all constituent dipoles. At a particular temperature referred to as Neel's temperature there is an emergence of the antiparallel configuration. This causes the magnetic susceptibility to reach its peak value followed by a subsequent decrease[24].
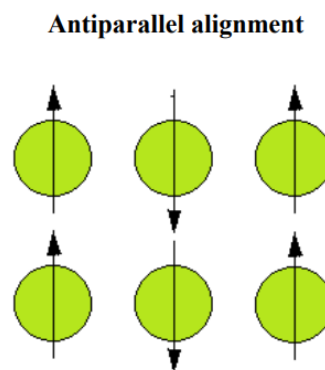
Figure 5 phenomenon of Antiferromagnetism [24]

2.1.5 Ferrimagnetism

Some ceramic materials exhibit ferrimagnetism type of permanent magnetization. Ferrimagnetic materials are characterized by cations that occupy distinct crystallographic sites and undergo antiferromagnetic coupling. As a result, the magnetization of two sublattices is antiparallel to each other, as shown in Figure (6). Despite this the net magnetization remains non-zero owing to the unequal strength of the two magnetizations. Because of unique properties these material get attention and are highly suitable for application in high-frequency and specialized magnetic devices[24].
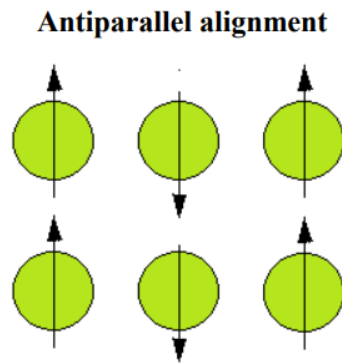
Figure 6 Ferrimagnetism behavior [24]

2.2 Dielectric behavior of materials

The reaction of electrons in material to the electric field applied in terms of polarization determines a material's dielectric behavior. Materials with dielectric properties are insulators that are not easily conductors of electric current and a variety of properties define their ability to respond to an electric field. Therefore, we can categorize the dielectric materials by the arrangement of their dipoles in relation to one another. A thorough explanation of the various polarity types is provided below.

2.2.1 Electric polarization

A dielectric material undergoes polarization once an electric field is applied to it. This indicates that the material's charges possibly modify one another producing electric dipoles. Such dipoles line in with the applied field, causing the material to become polarized electrically. Such polarization can be seen in fundamental dielectrics like diamonds and inert gases like Helium, Neon, Argon[25].

2.2.2 Ionic polarization

Ionic polarization is the term used to describe the process that takes place in some materials when they are placed in an external electric field. It is a kind of polarization that develops because of the migration of ions inside the lattice structure of the material. Electrostatic forces often hold the positive and negative charges together in a solid object such as an ionic crystal or a polar molecule. Positive and negative ions are moved away from their equilibrium positions and creates dipole moment in the vicinity of an

applied electric field. Alkali halides have the potential of exhibiting this polarization [25].

2.2.3 Orientation polarization

When dielectric materials are subjected to an external electric field a particular kind of polarization termed orientation polarization also referred to as dipolar polarization takes place. Individual molecules or atoms within a dielectric material may become electrically polarized when it is exposed to an electric field. In a nutshell, a net dipole moment results from the material's dipoles aligning due to the electric field. The outcomes of orientation polarization are often stronger in materials with high dipole moments and low alternated freedom of motion. The few dielectrics that exhibit this form of polarization are inorganic oxides like Silica or Quartz, Ceramics like Porcelain and Polymers like polyvinyl Chloride [25].

2.2.4 Interface and space charge polarization

An electric dipole moment is produced at the interface between two dielectric materials that are not identical to one another because of the rearranging of charges there is known as interface polarization. A particular kind of polarization known as "space charge polarization" takes place in dielectric materials like insulators and the dielectric layers of capacitors. Whenever an electric field is placed next to a dielectric substance, the material's electrons are slightly moved from their initial equilibrium positions, producing positive and negative charges. The negative charge carriers are pushed in the reverse direction, the positive charge carriers are drawn in the direction of the applied electric field. It is common for charges to collect along the boundaries of material grains which results in both interface polarization and space charge polarization. In spinel ferrites both these polarizations could be found [25].

2.3 Dielectric properties

The electrical characteristics of materials that govern their ability to respond to an electric field are referred to as dielectric properties. Dielectric characteristics primarily consist of tangent loss, ac conductivity, impedance and dielectric permittivity which is also known as dielectric constant and losses. If applicable these dielectric properties have a substantial effect on the application of these materials for EMI shielding which act as an insulating barrier and block the passage of EMI signals [ref]. These

characteristics can also be used to learn more about the process by which the material's electric field is produced. For easier understanding, a summary of these qualities will be provided in the sections that follow.

2.3.1 Dielectric permittivity

The capacity of a material to store energy and polarize in an electric field is permittivity. It can be explained using an equation (1).

$$\varepsilon = \varepsilon' - j\varepsilon''$$
$\qquad\qquad$…..(1)

whereas the polarization capability is represented by real part (ε') and stored energy of dielectric constant, whereas the (ε'') represents the energy losses of dielectric loss. The formula can be used in determining the dielectric constant in below eq (2).

$$\varepsilon' = \frac{Cd}{\varepsilon_\circ A}$$
$\qquad\qquad$…..(2)

Where ε' denotes a material's permittivity which indicates its capacity to store charge, C stands for capacitance in farads, its thickness is d, cross-sectional area of the pellet's is A and $\varepsilon_\circ$ for the constant of free space permittivity, which has a value of 8.85×10^{-12} F/m. Using below equation (3), the dielectric loss that is associated with the calculation of loss of energy.

$$\varepsilon'' = \varepsilon' \times D$$
$\qquad\qquad$…..(3)

While material dielectric loss is ε'' and D is the dissipation factor.

2.3.2 Tangent loss

The ratio between dielectric material's loss part (dissipated energy) and its storage part (stored energy) is known as the tangent loss or delta. It is expressed as the difference between the imaginary and real parts of the dielectric constant (ε' and ε''). By using the formula shown in equation (4) the tangential losses can be calculated.

$$tan\delta = \frac{\varepsilon''}{\varepsilon'}$$
$\qquad\qquad$…..(4)

2.3.3 Ac conductivity

The physical characteristic describes the conductivity of a material within it is known as conductivity. The equation (5) can be used to compute the Ac Conductivity

$$\sigma_{AC} = \varepsilon_o\, \varepsilon''\omega\, tan\delta \qquad \text{here } \omega \text{ is } 2\pi f \qquad \text{.....(5)}$$

Typically, AC conductivity is denoted by the Greek letter (σ_{AC}), where omega (ω) stands for the angular frequency. ε_o is the permittivity of free space, while the dielectric permittivity is represented by ε''

The relationship between the frequency and AC conductivity (ac) is shown by the general relationship presented below equation (6), which is based on the literature.

$$\sigma_{total}(\omega) = \sigma_{dc}(T) + \sigma_{ac}(\omega,T) = \sigma_{dc}(T) + B\omega^n \qquad \text{.....(6)}$$

where $\sigma_{dc}(T)$ stands for the DC conductivity independent of frequency contributing in the conduction band, the pure AC conductivity which is frequency-dependent contribution of the electron hopping at the B sites is known as $\sigma_{ac}(\omega,T)$, B is the conductivity-related pre-exponential constant and n stands for the temperature-dependent frequency component.

2.3.4 Impedance dielectric

When analysing the properties of dielectric materials, impedance refers to the resistance that the dielectric faces in an alternating current circuit. The phenomenon of Dielectric impedance happens as a consequence of the capacitive properties of the dielectric material when a dielectric is subjected to an AC voltage. The phenomenon under consideration leads to the alignment of the dielectric molecules or atoms, inducing a state of polarization, which ultimately generates the accumulation and discharge of electrical potential. The electrical resistance offered by a dielectric substance is influenced by both its capacitance and frequency that alternates the current signal. The expression for the impedance of a dielectric material can be denoted by the subsequent equation (7):

$$Z = 1 / (j\omega C) \qquad \text{.....(7)}$$

Here, Z signifies the impedance, j denotes the imaginary unit ($\sqrt{(-1)}$), ω is angular frequency for alternating current, while C represents the capacitance of dielectric material. Impedance investigating the dielectric response of a complex, resistant material in relation to frequency. The technique's application and characteristics are contingent upon the chemical composition, structure, distribution of additives, and imperfections of the material.

2.4 Ferrites

Ferrites are a particular kind of material that has unique property of being both magnetic and insulating in nature [4]. Ferrites have been essential to the growth of the technology-based industry since the middle of the 20th century. Ferrites, generally referred to as ceramic compounds which is composed of Iron oxide (F_eO) along with other metallic elements including Mg, Zn, Cu, Ni, Mn etc. Due to their composition and structure ferrites have high electrical resistance which allows them to behave as insulators and display magnetic behavior. As a result, they are unique and desirable for a range of industrial applications, especially in almost any present electronic equipment. Great interest has always existed in ferrites that are frequently used in magnetic storage devices, data storage, recording medium and transformers because of their unique combination of magnetic permeability and dielectric permittivity. ferrites are divided into soft and hard ferrites based on their magnetic property.

2.4.1 Soft magnetic ferrite

The class of soft ferrites having low coercivity and assumed to be brittle includes ferrites that quickly alter their magnetization and demagnetization in the existence of magnetic field. It remains magnetic when being affected by a magnetic field. Their magnetic properties result from an interaction between ions that are situated in different positions within the crystal structure with respect to oxygen ions. Soft ferrite material is believed to be semiconductor because of its electrical characteristics. The hysteresis loop area and coercivity value are quite small for soft ferrites. This indicates that ideally, ferrite would have low coercivity with no hysteresis loss negligible remanence, high saturation magnetization and high permeability.

2.4.2 Hard magnetic ferrite

Hard ferrites are also referred to as magnets made of ceramic. After the applied field is removed, hard ferrite material continues to maintain its magnetization. Hard magnetic materials have large hysteresis loop and a high value of coercivity. In addition, there are often two alternative approaches for obtaining hard magnetic materials. One approach involves shaping them into the desired shape, sintering them, and then magnetizing them so they may be used as ring magnets and motors. In contrast, they can also be formed before the sintering process in the presence of a magnetic field. Such

hard magnets exhibit powerful magnetism and are mostly employed in electric automobiles and refrigerator magnets.

2.5 Dielectric properties of spinel ferrite.

Dielectric properties, i.e., dielectric constant, loss tangent loss, and AC conductivity of Spinel ferrites can be changed by substituting metallic cations. The dielectric behavior of Mg ferrite may be increased by using metallic cations like Mg and Zn. This alteration has the potential to aid in the determination of the utilization of materials. Materials possessing low dielectric constants are of great utility in EMI shielding applications.

Spinel ferrites are a good choice of material for EMI-absorbing low-frequency range. $MgFe_2O_4$ has a high degree of permeability, strong chemical stability, high electrical resistivity, low cost [16-18]. The distinct dielectric characteristics of spinel ferrites are caused by the cubic phase pattern with an average crystallite size. These dielectric characteristics enhanced the absorbance of EMI shielding.

2.6 Application of ferrites

Ferrites are suitable for many important applications across several industries since they contain specific characteristics in EMI/RFI suppression, microwave applications, magnetic recording media etc [re]. The following are several prominent domains in which ferrites find application.

- Electromagnetic Interference shielding
- Permanent Magnets
- Magnetic Sensors
- Magnetic Core Materials
- Cathode ray tubes (CRTs) for magnetic shielding
- Ferrite antennas for AM radio reception
- Magnetic resonance spectroscopy
- Power supplies and electronic filters.

2.7 Classification of ferrites

Ferrites are just a mixture of (Fe_2O_3) and metallic ions (Mg, Zn, Mn, Ni, etc.). Fe_2O_3 is the predominant component. Different kinds of ferrites can be distinguished

by the molar ratio of Fe_2O_3 to other oxide components in these ceramic compounds. The ferrites can be subdivided into the following groups based on this combination:

- Spinel Ferrite
- Hexagonal Ferrites
- Garnet
- Ortho Ferrites

Table 1 Classification of Ferrites

Class	Molar ratio	Terminologies
Spinel	MFe_2O_4	M is a divalent transition metal ion
Hexagonal	$MFe_{12}O_{19}$	M is a divalent from group IIA.
Garnet	MFe_5O_{12}	
Ortho	$AFeO_3$	A specifies rare earth metal such as Tb, La, Nd, Y, Sc

2.7.1 Spinel ferrite

A group of materials having a spinel structure are commonly referred to as spinel ferrite. These substances are a subset of ferrite which are ceramic materials made of iron oxide (F_eO) with one or more other metal oxides, for example, aluminum oxide (AlO) or magnesium oxide (MgO). Spinel ferrites have the general chemical formula M Fe_2O_4, whereby M stands for a divalent metal ion. Magnetite (Fe_3O_4), the most well-known and widely used spinel ferrite is one of the spinel ferrites that are frequently studied along with other compounds including magnesium ferrite ($MgFe_2O_4$), zinc ferrite ($ZnFe_2O_4$), and cobalt ferrite ($CoFe_2O_4$). Since these substances have ferrimagnetic characteristics and a net magnetic moment despite this, the direction of the magnetic dipole of the iron ions in one sublattice is different from that of the moments in the other sublattice. Spinel ferrites exhibit magnetic behavior due to this configuration, which generates a non-zero magnetic moment. They are versatile materials in a number of industrial applications because of their special assortment of magnetic properties, including large coercivity and exceptional chemical resistivity.

Spinel ferrites have remarkable magnetic and electrical characteristics which lend them beneficial in a variety of applications including high-frequency transformers, microwave devices, telecommunications, and electronics.
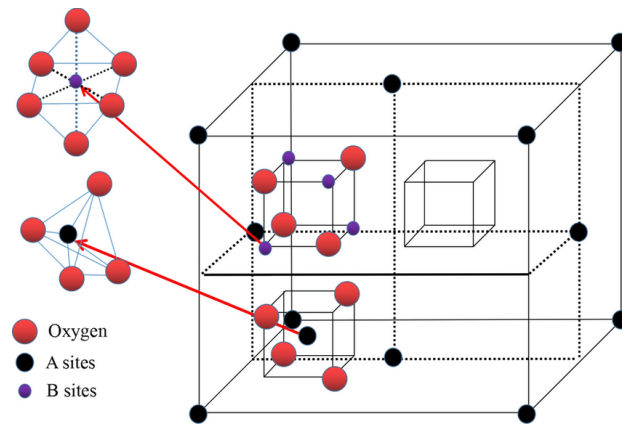
Figure 7 Structure of spinel ferrites

2.7.2 Hexagonal ferrites

They are a particular kind of ferrite known as hexaferrite that has hexagonal crystal structures. $MFe_{12}O_{19}$ is the typical chemical formula for hexagonal ferrites, where "M" stands for a divalent metal cation like barium (Ba), or strontium. Metal cations and iron oxide (Fe_2O_3) anions are arranged in multiple layers to form the hexagonal crystal structure. Since hexagonal ferrites are ferrimagnetic materials they are permanently magnetized even in the absence of an external magnetic field applied. Interesting magnetic characteristics, make hexagonal ferrites to be beneficial in a wide range of applications.
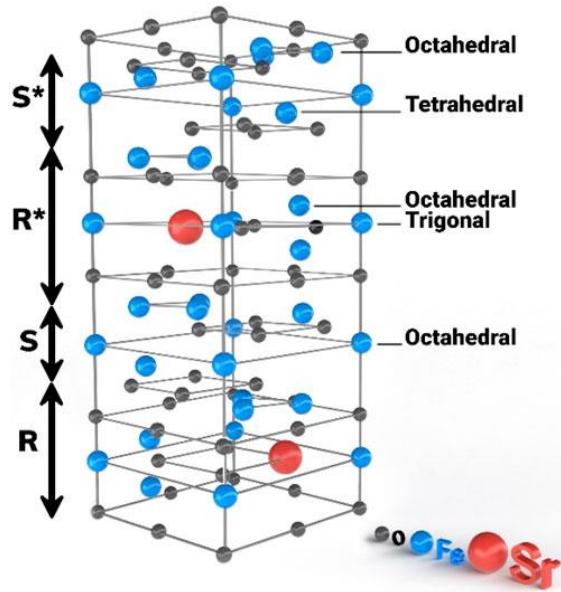
Figure 8 Hexagonal ferrite's structure

2.7.3 Garnet

In addition to spinel ferritesother significant forms of ferrites are garnets, which have a standard formula $M_3Fe_5O_{12}$. M is a divalent metal ion that comes from any of the magnetic rare earth elements including Ytterbium and Lanthanum. Similar to spinel ferrites, garnets have the same characteristics that can likewise be altered by replacing any Yttrium or iron ion with any rare earth ions. Garnet has an orthorhombic crystal structure. Tetrahedral, octahedral, and dodecahedral sites are just a few of the possible locations for the trivalent cation. Although the iron in spinel's is capable of being divalent or trivalent, all garnets display high resistivity and are valuable for high frequency uses since all rare earth elements are invariably trivalent which restricts the electron hop procedure.
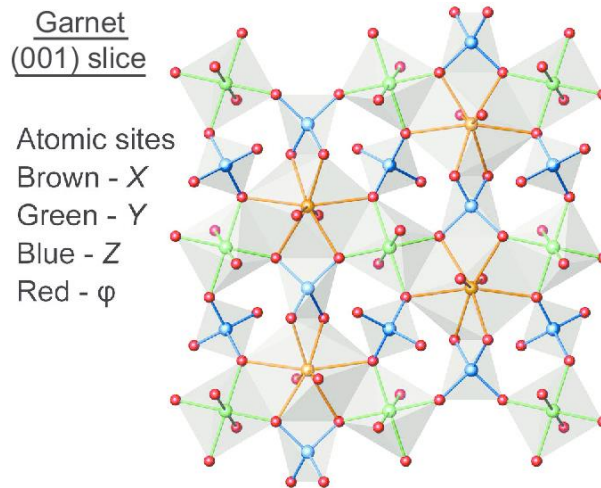
Figure 9 Structure of Garnet ferrites

2.7.4 Ortho ferrites

The word "ortho ferrite" refers to the crystal structure rather than any specific composition or combination. Three uneven axes that are at right angles to one another make up orthorhombic crystals. The metal ions included in the crystal lattice and their order determine the characteristics of an ortho ferrite. Ortho ferrites have good magnetic characteristics that is high permeability at high frequencies, high electrical resistivity and low eddy current losses. Due to these qualities, they are useful in applications for magnetic, electrical, and telecommunications equipment.
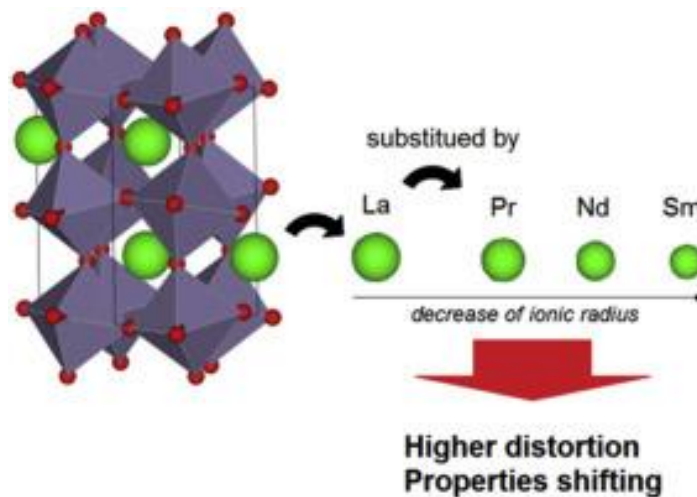
Figure 10 Ortho ferrites Structure

2.7.5 Mixed spinel ferrites

One sort of crystal structure that can be seen in some materials is referred to as a mixed spinel. A mixed spinel has two distinct cations (ions with a positive charge) occupying its crystal lattice. It has a typical chemical formula AB_2O_4, while A and B stand for two distinct metal cations. Oxygen ions (O^{2-}) get enclosed by a mixture of A and B cations to form the crystal lattice. These cations may vary in atomic size and ionic charge inside the crystal lattice. According to the material, the variation may be random or organized. The arrangement can also be affected by thermodynamic laws, giving rise to particular crystal formations which are called inverse spinels or normal spinels. For instance, chemical formula of zinc ferrite (ZNF) is $(Zn2+)_A$ $[Fe_2^{3+}]_B$ O_4 and has a normal spinel structure lattice that represents a preferable group of nanoscale ferrites and has improved chemical activity, and thermal stability. Along with ZNF, magnesium ferrite (MGF), which has an inverted spinel structure and the chemical formula of $(Fe^{3+})_A$ $[Mg^{2+}\ Fe^{3+}]_B$ O_4, is another exceptional member of the ferrites group owing to its superior magneto-electric capabilities. The Zinc ferrites and Mmagnesium Ferrites are both useful in the fields of electronics and biomedicine [22,23]. Therefore, a mixed spinel lattice structure is created by the combination of two different lattice structures, namely ZNF (normal spinel) and MGF (inverse spinel), which have better qualities than either of their individual components. Due to the interaction of several distinct cations, mixed spinels can display remarkable, optical electrical, and magnetic characteristics.

The objective of this research is to better understand mixed-type spinel ferrite in the next sections.

2.7.5.1 Structure of mixed spinel ferrite

Mixed spinel ferrites are a subset of materials that are classified under the spinel ferrite family, a group of magnetic oxides. These ferrites possess a comprehensive chemical formulation of $A_1A_2BO_4$ where the tetrahedral sites or A-sites consist of a combination of two distinct divalent metal cations, namely A_1 and A_2. On the other hand, the octahedral sites or B-sites comprise a trivalent metal cation B. The heterogenous grouping of metallic cations provides a capacity for engineers to modify the characteristics of ferrite material for targeted purposes. The composition of mixed spinel ferrites is founded on the spinel crystal structure, which is an FCC (face-cantered cubic) lattice.

2.8 Synthesis techniques

Methods used to synthesize a desired material or chemical are known as synthesis techniques. The proposed material's characteristics and the desired result determine the precise synthesis process that is utilized. The following are some typical synthesis methods utilized across multiple fields:

• Sol- Gel Technique

• Hydrothermal Technique

• Chemical Vapor Deposition

• Chemical Co-Precipitation

• Sono-Chemical Technique

• Mechanical Alloy Technique

• Micro-Emulsion Technique

The mixed spinel ferrite nanoparticles were synthesized in the current study utilizing the sol-Gel technique. Accordingly, just this technique will undergo extensively addressed in the next section.

2.8.1 Sol- Gel combustion technique

Sol-gel combustion is a well-liked technique for creating a wide range of oxides in various forms (gels, powders, particles, etc.). Fundamentally, the sol gel combustion process requires two stages for the systematic formation of materials. A sol-gel precursor mixture can be produced in the first stage through the combination of metal salts or organic molecules with the appropriate solvent. The precursor solution's composition, stoicism, and uniformity can be precisely controlled by the sol-gel process, resulting in the production of materials of excellent quality. The second phase, known as combustion formation, involves a regulated exothermic response of the sol-gel precursor solution. The precursor solution is heated to an elevated temperature in order to start the combustion process, which causes an immediate emission of gases and the development of a self-sustaining combustion centre. A tremendous volume of energy is released during the exothermic reaction which encourages the material of choice to expand and crystallize quickly.

2.8.2 Advantages of sol-gel technique

Furthermore, compared to traditional synthesis methods, the Solgel combustion approach has a number of clear advantages.

• First off, it is a straightforward and economical procedure that can be carried out with reasonably cheap equipment enabling access for researchers with different resources.

• As a result of the method's excellent adaptability, materials may be produced in huge quantities, which is extremely important for industrial applications.

• Sol-gel combustion technique is made possible Purity and homogeneity at the molecular structure

• Sol-gel process is exothermic due to its high reaction rates the combustion reaction happens quickly. Massive manufacturing and applications that require immediate attention benefit from this.

• Narrow particle size distributions of the synthetic materials are frequently produced using the sol-gel combustion process. it results in consistent characteristics and enhanced efficiency.

• Due to the ease of the procedure and the accessibility of precursor components. Sol-gel combustion has the potential to be scaled up for industrial use.

2.8.3 Applications of Sol-Gel technique

The excellent qualities of the materials produced by the sol gel combustion technique make them extremely popular for a variety of technical applications. Due to their characteristics, they are used in a variety of applications, including power storage batteries and supercapacitors, gas sensing, ecological clean-up, photovoltaic cells, and biological ones as well.

Chapter:3

Materials Synthesis and Characterization

This chapter provides thorough explanations of the experimental and characterization methods used to fabricate and analyse the samples. The synthesis method of sol gel combustion was employed for of Mg-Zn ferrite, while the incorporation of aluminum nano particles into the ferrite was achieved through ball milling.

3.1 Materials

In the synthesis of mixed spinel ferrite, the chemicals employed were of a purity level equal to or greater than 99%. These ingredients were utilized without further any additional purification. The preparation of solution was done in deionized water, commonly referred to as DI water. The suppliers of the chemicals were none other than Sigma Aldrich. A detailed account of these chemicals utilized in the process can be seen in Table 3.1, which is located below.

Table 2 List of elements and their formulas

No of chemicals	Chemical's name	formula	Molecular weight
1	Magnesium nitrate hexahydrate	$Mg(NO_3)_2.6H_2O$	256.41 gmol
2	Zinc nitrate hexahydrate	$Zn(NO_3)_2.6H_2O$	297.49 gmol
3	Zinc nitrate	$Fe\,N_3\,O_9.H_2O$	404.00 gmol
4	Citric acid	$C_6\,H_8\,O_7$	192.1 g/mol
5	Aluminum	Al	26.98 g/mol

3.2 Experiment data

Different samples of the spinel ferrite have been obtained utilizing the sol-gel method. Magnesium was substituted to the zinc ferrite [$Mg_{(x)}Zn_{(1-x)}Fe_2O_4$] in the following concentrations:

1. x= 0.1
2. x = 0.25
3. x = 0.50
4. x = 0.75
5. x = 0.90

An estimate of the mass of the solvents was obtained by using the mathematical expression described in equation (8):

$$mass\ (g) = \frac{molarity \times molecular\ mass \times 100}{1000} \qquad .....(8)$$

The synthesis of the materials will be further discussed in the chapter that follows.

3.3 Synthesis of mixed spinel ferrite

Mg- substituted Zn ferrites [$Mg_{(x)}Zn_{(1-x)}Fe_2O_4$] were synthesized using the auto-combustion sol-gel method. The analytical grade starting precursors, Magnesium nitrate Citric acid [$C_6H_8O_7.H_2O$] having purity up to 99.99% were outsourced from Sigma Aldrich. Using the formulas $Mg_xZn_{(1-x)}Fe_2O_4$, all of these chemicals were synthesized in the appropriate stoichiometric ratio. All the sample compositions were adjusted according to the stoichiometric formulas $Mg_xZn_{(1-x)}Fe_2O_4$ where x= 0.10, 0.25, 0.50, 0.75, and 0.90.

These precursors were dissolved gradually in deionized water while being magnetically stirred along with the chelating agent citric acid ($C_6H_8O_7H_2O$). The required quantity of Ammonia was added dropwise in the solution media to maintain the pH level at 7 Figure (11).

Figure 11 The action of chemical heating and stirring is depicted.

Eventually, a relatively transparent gelatinous solution with a light red colour was obtained. Ammonia addition was stopped at this point and the solution was stirred at 80°C continuously for approximately 3 hours to evaporate the water present in the solution and transformed it into a viscous dark grey gel depicted in Figure (12).

Figure 12 The action of solution transformed in viscous dark grey gel

On the completion of water evaporation upon heating, the viscous gel started to expand occupying a large volume followed by releasing of gasses in form of dense fumes. The gel was produced through flameless auto-combustion reaction that began from the bottom up, much like a volcanic eruption Figure (13).

Figure 13 Displays the appearance of flameless auto-combustion.

Upon air cooling of the reaction products, the obtained sample was crushed into a fine powder with the help of a motor and pestle Figure (14).

Figure 14 Mixed spinel ferrite powder after sintering

Further, the powder sample was sintered in a muffle furnace at 750 °C for one hour [26]**.**

3.4 Characterization techniques

Utilising XRD, SEM, and LCR metre the synthesised samples were characterised**.** The following sections provide a summary of the tools and samples that were prepared for characterization:

3.4.1 Scanning electron microscope

SEM is an effective imaging technique that can be used effectively to instigate the surface morphology and structure of various samples at a high resolution.

Working principle:

An electron gun is used by the SEM as its electron source. By providing a voltage to a filament, the gun generates a high-energy electron beam. The electron beam is accurately accelerated and concentrated to create a narrow, converging beam. A series of electromagnetic lenses that the beam is steered through control and refine the direction of the electrons. Through this procedure, the beam is kept properly focused and is carefully controlled as it scans the sample surface. The surface of the specimen under examination is purposefully targeted by the concentrated electron beam. When the electrons collide with the specimen's atoms, a variety of interactions occur, ultimately leading to the creation of signals that provide important details about the specimen's surface. Secondary electrons (SE) and backscattered electrons (BSE) are the two main categories of signals that are frequently seen in SEM. A portion of the electrons are released from the sample's surface (SE) when the primary electron beam collides with it, while the remaining electrons are redirected back in the direction of the electron cannon and are referred to as BSE. SE and BSE signals can be collected by detectors that have been placed carefully above the sample. The BSE detectors can provide insightful information on the sample's composition and atomic number, whereas the SE detectors are generally used to provide high-resolution images that can reveal the sample's surface topography. The SEM system uses the grayscale intensity values generated from the detector signals to produce a visual representation of the sample's surface. This image provides a detailed and high-resolution perspective of the surface characteristics.
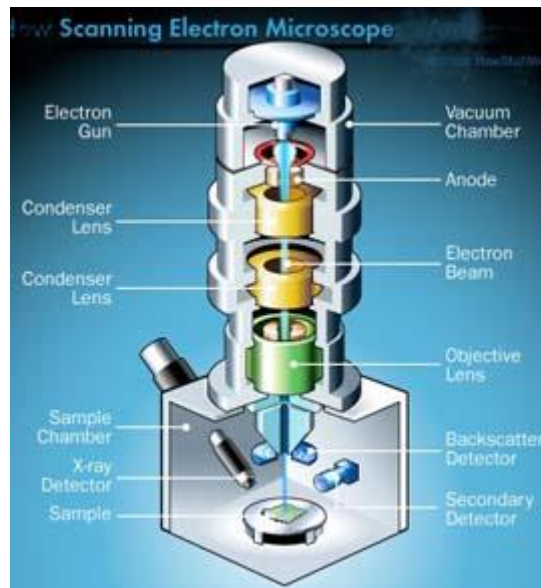
Figure 15 Working of scanning electron microscope.

3.4.2 XRD

An effective analytical technique used in analyzing crystal structure of materials is XRD. The X-ray diffraction phenomenon, which results from an interaction between X-rays and the atomic structure of a crystalline substance, forms the basis for how XRD works. The following are the XRD operating principles:

The monochromatic X-ray source used in XRD is often created by exposing electrons to a metallic target, such as copper or cobalt. The target material chosen determines the specific wavelength of the produced X-rays. The material that needs to be assessed is transformed into a tiny powder or a thin membrane. To ensure that the X-rays fully penetrate the substance and interact with its crystalline formation, the specimen must be in a pulverized state. The incidence or Bragg angle refers to the direction at which monochromatic X-rays from the source are directed towards the sample. X-rays interact with the electrons encircling the atoms in the crystal lattice of the sample, scattering them in different ways. X-ray diffraction is the term used to describe this phenomenon.

The distance between the atoms in the crystal lattice determines the diffraction pattern produced by the dispersed X-rays. According to Bragg's law, constructive interference must meet the following conditions in order for the X-rays to experience constructive interference and produce a diffraction peak:

$$n\lambda = 2d \sin(\theta) \qquad \qquad .....(9)$$

A detector collects the diffracted X-rays that is positioned antiparallel to the incoming X-ray energy. The tool records the X-rays' diffraction intensity in respect to their diffraction angle (2θ). The recorded diffraction pattern is then examined to determine the positions and peak intensities. The crystal structure of the sample can be recognized and characterized by comparing the recorded diffraction angles to documented values for distinct crystalline materials.
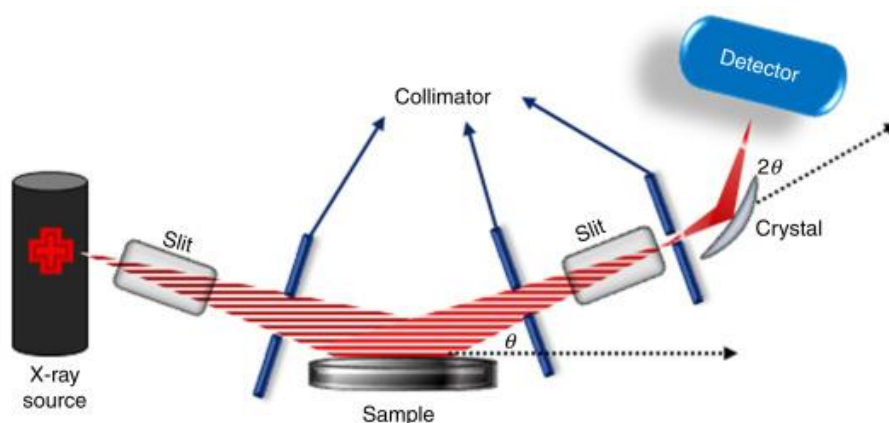
Figure 16 Schematic of XRD working.

XRD is extensively employed in the realm of materials science, geology, chemistry, and diverse other disciplines to discern crystal structures, recognize phases, scrutinize crystal imperfections, and probe the composition of materials in both research and industrial contexts.

3.4.3 FTIR

To identify and examine the functional groups and molecular vibrations that are present inside a particular sample, FTIR is a powerful analytical tool. A wide spectrum of infrared radiation is produced by an infrared light source, which is used in FTIR. This particular infrared spectrum has a wide range of wavelengths that match the molecular vibrations of various functional groups that are present in the sample. The sample can be prepared by making a thin film or an opaque pellet. Depending on the characteristics of the sample and the precise information that must be obtained through analysis, a particular method for sample preparation is chosen. The light that the sample either transmits or absorbs is collected and combined with an infrared reference beam. The interferometer is then used to pass this composite beam. The resultant beam undergoes both constructive and destructive interference in the interferometer, which results in the creation of an

interferogram. The interferogram, in turn, acts as a database for knowledge about the combined beam's intensity in respect to the optical path difference. The infrared spectrum produced shows distinct peaks at wavenumbers (the inverse of wavelength) that coincide with the vibrational frequencies of the specimen's molecular bonds. Notably, each bond type and functional group causes its own distinct collection of infrared spectrum peaks to be produced. To find out the chemical structure and functional groups present in the specimen, the recorded infrared spectrum is compared with spectral databases or reference spectra.
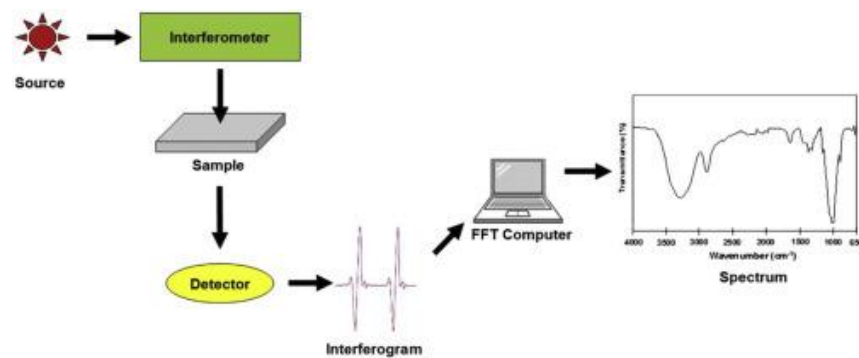
Figure 17 Working principle of FTIR.

3.4.4 LCR

The term "LCR, impedance analyzer" refers to a class of electronic measuring equipment known as an LCR meter or "Inductance-Capacitance-Resistance" meter. Its main objective is to determine the electrical properties of inactive electronic components such inductors (L), capacitors (C), and resistors (R).

A sinusoidal test signal with a specified frequency, typically ranging from a few Hertz to many Megahertz, is produced by the LCR meter. A capacitor, resistor, or an inductor may be the component under examination at this point.

The voltage and current responses of a specific component to the applied test signal are determined using the LCR meter. It is important to note that while the voltage and current are always in phase for resistors, this is not the case for inductors and capacitors because of their reactive nature.

The LCR meter evaluates the phase angle, which reveals the nature of the component under consideration (whether it is an inductor, capacitor, or resistor) by

measuring the phase difference between the voltage supplied and the current generated.

The LCR meter uses voltage and current measurements to perform computations to calculate the impedance of an electrical component. Impedance is defined by a complex value that represents the component's resistance and reactance (inductive or capacitive). The computed impedance is displayed on the screen of the LCR meter, together with other relevant details such as phase angle, capacitance, inductance, and resistance.

3.4.5 VNA

VNA is a sophisticated electronic measurement device used to characterize and evaluate the operational efficiency of high-frequency and radiofrequency (RF) components, circuits, and systems. For testing purposes, VNA generates a signal in the form of a continuous-wave (CW) or swept-frequency wave. This signal has a carefully specified frequency range and resolution. The frequency range of the VNA can range from a few megahertz to several Gigahertz, depending on its individual capabilities. The S-parameters, which are complex-valued quantities used to describe the electrical behavior of the DUT with respect to reflection coefficient (S11 and S22) and transmission coefficient (S21 and S12) at various frequencies, are determined by analyzing transmitted and reflected signals using the VNA. In RF and microwave engineering, vector network analyzers are essential tools for the design, testing, and resolution of various RF components, antennas, filters, amplifiers, and communication systems. By serving as vital instruments for designing, testing, and debugging a variety of RF components, antennas, filters, amplifiers, and communication systems, the Vector Network Analyzers serve a crucial role in RF and microwave engineering.

Chapter:4

Results and Discussions

4.1 Details study of Structure and composition optimization on dielectric properties and electromagnetic interference shielding of Mg-Zn spinel ferrites.

4.1.1 Structural and phase studies

Figure (18) illustrate the X-ray diffraction spectra that were plotted to study the structure and phase purity of synthesized samples $Mg_x Zn_{(1-x)} Fe_2O_4$ (x = (0.1, 0.25, 0.50, 0.75, 0.90). The single-phase cubic structure that formed was confirmed by the polycrystalline patterns present in all samples with the standard JCPDS card (01-086-1345) in the scanning range of 20 to 80 degree. Each of these peaks can be indexed as the crystallographic planes of (220), (311), (400), (422), (440), and (533) at 2θ values in line with Bragg's Law of X-ray Diffraction. The patterns exhibit sharp and intense peaks along the specified crystal planes are present in all the samples.
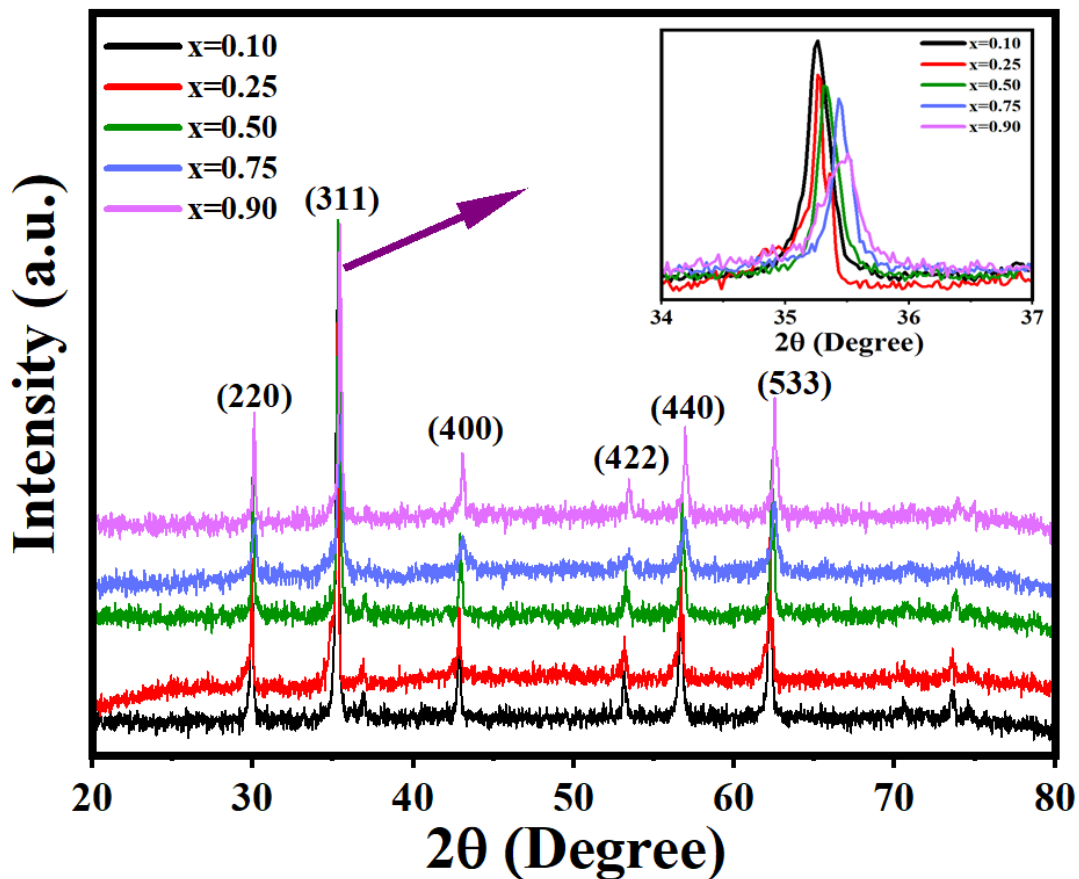
Figure 18 XRD spectrum and fluctuation of highly intense peak (311) of synthesized $Mg_{(x)}Zn_{(1-x)}Fe_2O_4$ (x= 0.1, 0.25, 0.5, 0.75, 0.90) nanoparticles.

It is observable that the diffractograms showed a gradual decrease in peak intensities, which demonstrates that as magnesium content increases, the percentage of the crystalline structure of the zinc ferrite is decreasing. XRD data were used to calculate several standard structural parameters. The Debye Scherrer relation (Eq 10) was used to calculate the average crystallite size (t) of the prepared samples using the value 2θ and full width at half maximum (FWHM) values related to the most intense peak having plane (3 1 1). The average size of crystallites was in the range of nanoscale i.e., between 67nm to 39nm. Figure 20 (a) indicates the compositional variations of crystallite size values in relation to the Mg^{2+} substitution. It is visible from Figure 20 (a) that average size of crystallites declines linearly, by increasing Mg^{2+} content, and shift in the peaks toward right side and widening of diffraction was also observed. Table 3. summarizes the obtained average crystallite values (t). An obvious peak broadening with increasing concentration of Mg^{2+} may also be seen when studying the most intense peak (311). The widening of the diffraction peak, which is seen in Figure (18). can be associated with the distribution of crystallinity that results in the lattice strains.

$$t(311) = \frac{K\lambda}{\beta \cos\theta} \qquad \qquad .....(10)$$

Here t is the average particle, λ is the X-ray wavelength (0.1542nm), β is FWHM, and θ is the Bragg angle of the (311) plane.

The values of the lattice constant (a) were calculated using the Miller indices (h, k, l) and interplanar spacing (d) as stated in the formula below.

$$a = d\sqrt{h^2 + k + l^2} \qquad \qquad .....(11)$$

Figure 20. (a) illustrates the variation in the lattice constant (a) in regard to the substitution of Mg^{2+}. The value of the lattice constant (a) decreases significantly with an increase in concentration of Mg^{2+} ions in $Mg_xZn_{(1-x)}Fe_2O$ ferrites. Mg^{2+} ion replaces Zn^{2+} ion in the spinel ferrite $[Zn]_A [Fe_2]_BO_4$, as Mg^{2+} ion primarily occupies the octahedron (B) site while Zn^{2+} ion mainly occupies the tetrahedron (A) site [27]. By substituting the Mg^{2+} ion, it is observed that the lattice significantly shrinks. By taking into consideration Through below equation cation conversion of Mg-Zn ferrites was explained

$$[Zn^{2+}] + [Fe^{3+}] \rightarrow [Mg^{2+}] + Zn^{2+} + Fe^{3+}$$

When considering the ionic radii of Mg^{2+} and Zn^{2+}, such behaviour might be explained. The ionic radii of Mg^{2+} is 0.66 A ° less than those of Zn^{2+} when Mg^{2+} is substituted with Zn^{2+} (0.82 A °)[28]. It has been found that this smaller cation substitution occupies interstitial sites which leads the lattice to shrink and reduced in size [29]. Due to a change in ion radius substitution, the peak in the XRD pattern shifts to a higher 2θ value, the lattice parameter will reduce from 8.43 A° to 8.40 A° this whole phenomenon can be explained by Vegard's Law. According to Vegard's law, the substitution of different ions changes in ionic radii and replacing ions for spinel system led to the linear change in lattice parameter. A similar deteriorating trend of the lattice constant was found in the literature [30]. Values of the lattice constant were utilized in the following common formula to calculate the unit cell volume "V" of the manufactured samples.

$$V = a^3 \text{ Å}^3 \qquad \qquad .....(12)$$

Since the unit cell volume has direct relation with the values of lattice constant, they follow the same pattern. As the number of substitutions rises, the unit cell volume values exhibit the same pattern and indicating that the values of the lattice constants are

directly proportional. The X-ray density (d_X) values were measured by utilizing the coordination number (Z) of the cubic lattice, the molecular weights of the constituents, volume (V) of the unit cell, and the Avogadro number (6.022×10^{23}).

$$d_X = \frac{Z \times M}{V \times NA} \; \text{gm/cm}^3 \qquad \text{.....(13)}$$

The measurements of X-ray density indicated a declining trend by increasing Mg^{2+} ions substitution [31]. The declining trend is due to variation in lattice constant and decrease in the molecular weight of the $Mg_xZn_{(1-x)}Fe_2O_4$ substituents as Mg^{2+} (24.305 amu) has smaller molar mass relative to Fe^{3+} (55.85 amu). Table 1. shows the calculated X-ray density values. Figure 3(b). demonstrates the effect of compositional variation on X-ray density (d_X) values. The following formula was used to determine the bulk density (d_B) values.

$$d_B = \frac{m}{\pi l r^2} \qquad \text{.....(14)}$$

$$P = 1 - \left(\frac{d_B}{d_x}\right) \qquad \text{.....(15)}$$

Here m is the mass, r is the radius, and l is the thickness of the pellet. Table 1. shows the calculated bulk density (d_B) values. Furthermore, Figure. 20(b) displays the compositional variability in bulk density (d_B). Like the density data from X-ray, and the bulk densities decreased as Mg^{2+} substitution increased. Also, it can be seen that values of bulk densities are significantly lower than density values obtained from X-ray data. The estimated porosity (P) fraction was calculated using the differential between the bulk and X-ray densities. The expected porosity fraction decreased with Mg^{2+} content, as seen in Table 3. Variation in porosity fraction with respect to composition is shown in Figure 20 (c)

$$L_A = \frac{1}{4} a\sqrt{2} \qquad \text{.....(16)}$$

$$L_B = \frac{1}{4} a\sqrt{3} \qquad \text{.....(17)}$$

The following equations were used to obtain the hopping length (L_A and L_B) values, which are tabulated in Table 3. The hopping length (L_A and L_B) values are demonstrating declining tendencies which are caused by the addition of smaller radii of Mg^{2+} ions. All above details are essential to comprehend as changing the ion distribution will vary the ion exchanges, and therefore affect the several properties like

structural and electrical of material. The SEM images of the synthesized nanoparticles for the compositions (x=0.1, 0.25, 0.50, 0.75, 0.90) are shown in Figure 19(a-e), respectively. The picture exhibits that with the rise in Mg concentration, the particles are equally dispersed and have a spherical geometry.

Figure 19 Scanning electron microscope images of $Mg_xZn_{(1-x)}Fe_2O_4$ nanoparticles with (a) x= 0.1, (b) x= 0.25, (c) x= 0.50, (d) x= 0.75 and (e) x= 0.90 at 0.5μ scale

Figure 20 Variation of crystallite size (t) and lattice parameter (a), (b) X-ray density (dX) and bulk density (dB) and (c) Porosity fraction with Magnesium ion concentration for synthesized $Mg_xZn_{(1-x)}Fe_2O_4$ (x= 0.1, 0.25, 0.5, 0.75, 0.90) nanoparticles

Table 3 Structural parameters including Lattice constant (A), Crystallite size (nm), Volume of the unit cell (A), X-ray density (gm/cm3), Bulk density (gm/cm3), Porosity Fraction (P), Tetrahedral Hoping length LA, Octahedral Hopping length LB

Composition (x)	a (A)	V (A)	t (nm)	d_X (gm/cm^3)	d_B (gm/cm^3)	P (%)	L_A (A)	L_B (B)
0.1	8.422	587.68	67.55	5.494	2.791	0.53	2.952	3.622
0.25	8.412	596.06	59.71	5.279	2.855	0.52	2.949	3.619
0.50	8.401	592.93	45.56	5.076	2.701	0.49	2.945	3.613
0.75	8.374	587.28	45.56	4.893	2.429	0.48	2.943	3.611
0.90	8.383	589.16	39.78	4.739	2.328	0.48	2.940	3.610

4.1.2 FTIR spectroscopy analysis

Figure.21 depicts the results of infrared spectral observations of Mg^{2+} replaced $ZnFe_2O_4$ that have been performed at room temperature in the wavenumber range of 400 cm^{-1} to

1000 cm^{-1}. Based on the Waldron categorization [31], two major absorption bands $v1$ and $v2$ were visible in each spectrum. These bands are associated with the stretching vibrations of the octahedral (B-O-B) and tetrahedral (A-O-A) metal-oxygen complexes, correspondingly. Ferrite having structure of single-phase spinel was formed, as indicated by the measured spectra for each Magnesium composition with $v1$ between (551 cm^{-1} to 566 cm^{-1}) and $v2$ between (424 cm^{-1} to 439 cm^{-1}) respectively. By oxygen's closest spatial structure, the two distinct sublattices where the metal ions are positioned in the ferrite are the tetrahedral (A) site and the octahedral (B) site. The tensile vibration of Fe^{3+} -O^{2-} is known as the absorption band identified near 550 cm-1 in the tetrahedron site, whereas the absorption band observed near 420 cm-1 is induced by the octahedral metal stretching [28]. The spacing between the A and B sites in the Fe^{3+} -O^{2-} could account for the variation in the positioning of the two absorption bands, $v1$ and $v2$ [32]. As shown in Table 4, when the concentration of Mg^{2+} is increased, the observed bands move from lower to higher frequencies, which is comparable with the inverse interaction between bond length and frequency band. The size of the unit cell decreases as the lattice parameter is reduced, which has an impact on the Fe-O position in a way that the lengths of the octahedral and tetrahedral bonds are decreased. Furthermore, Mg^{2+} also has smaller ionic radii, and its ability to fill both A as well as B sites with a high preference for B site occupancy that was mentioned in the preceding section. This means that the reduction around interatomic distance explains the shift towards an increase in frequency for both $v1$ around 650 cm-1, 700 cm-1, and $v2$ 900 cm-1. Additionally, in our spectrum, the peaks are seen to be significantly widened which is probably due to the increasing concentration of Mg^{2+} with low ordering as well as decrease in the amount of Fe-O bonds.
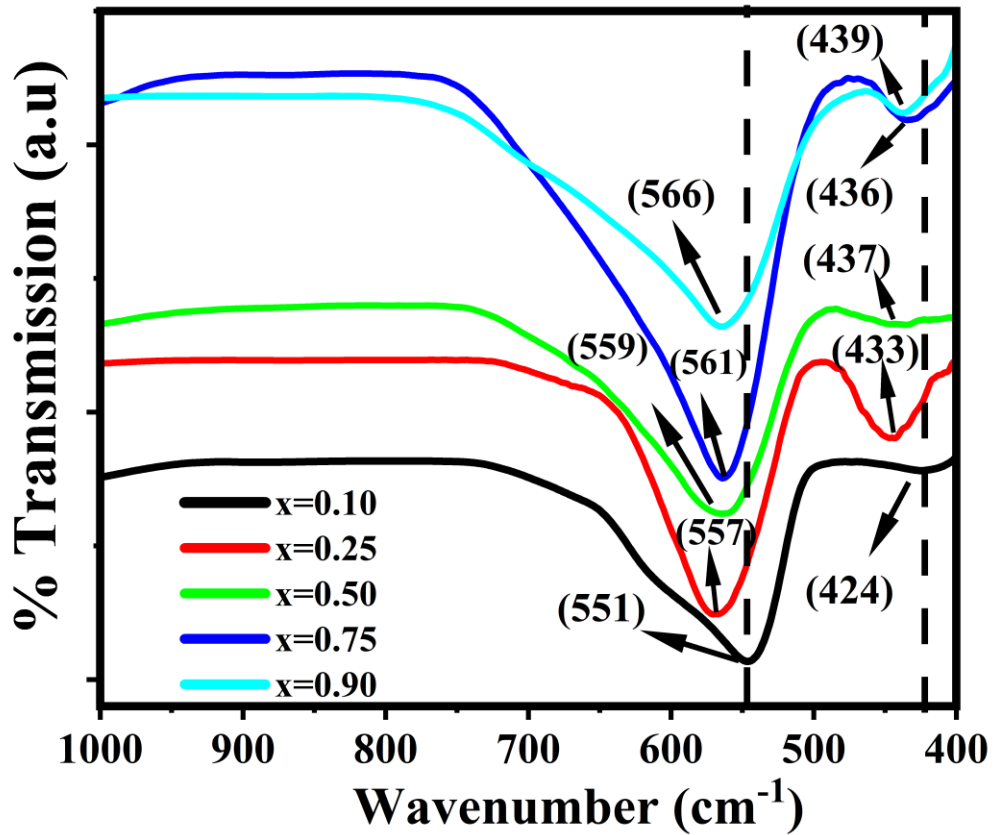
Figure 21 Fig. 4. Fourier transform infrared spectrum of synthesized $Mg_xZn_{(1-x)}Fe_2O_4$ (x= 0.1, 0.25, 0.5, 0.75, 0.90) nanoparticles in 400 to 1000cm-1 wave number range.

Table 4 Values of tetrahedral (v1) and octahedral (v2) band position of synthesized $Mg_xZn_{(1-x)}Fe_2O_4$ nanoparticles with respect to composition (x).

Compositions (x)	V1 (cm^{-1})	V2 (cm^{-1})
0.1	551	424
0.25	557	433
0.50	559	437
0.75	561	436
0.90	566	439

4.1.3 Dielectric constant.

The dielectric constant of ferrites corresponds to multiple parameters that represents the equation $\varepsilon = \varepsilon' - j\varepsilon''$, where the real part ($\varepsilon'$) which denotes polarization ability and energy storage and ε'' is the imaginary part that indicates the energy dissipation. Dielectric behaviour occurs due to dipolar, and interfacial polarization and its dispersion at low frequencies [33]. Various elements such as cationic distribution, method of synthesis, chemical homogeneity, structural variation, dopant substitution, powder density, and sintering temperature can affect dielectric performance. The value of the dielectric constant is shown in inset (5) to be highly dependent on the compositions (x) of the synthesized samples and the applied frequency. In contrast to the expanding frequency spectrum, the real part ε' of all the samples generally exhibits a pattern with the highest values in the low-frequency range. when the frequency increases the trend of the ε'(real part) of all samples exhibits smaller values until it almost reaches a point where it stagnates insignificantly. These large values of ε' at lower frequencies can be explained in simplified terms by the predominance of Fe^{2+} ions, accumulation of interfacial dislocations, oxygen vacancy defects and defects at grain boundaries. In comparison, the decreasing dielectric constant with rising frequency has resulted from the decrease in space charge polarization. This type of dielectric dispersion is explained with Koop's conceptualization principle that is relies upon the interfacial polarization of Maxwell-Wagner model [34]. This dispersion concept states that with the growth of polycrystalline ferrite, two distinct layers produce an inhomogeneous structure. The top layer contains well-conducting grains set apart over the second thin insulating grain boundaries with poor conducting properties. As a result, with ε' values in the low-frequency region, the ferrite therefore frequently exhibits good dispersed dielectric strong behaviour [35]. Additionally, during the sintering process Fe^{2+} ions accumulate from Fe^{3+} ions and become space charge carriers. The conductive boundary region is easier to observe at low frequencies whereby electron hopping between Fe^{2+} and Fe^{3+} causes a concentrated accumulation of electrons to occur. Space charge polarization is the consequence of these electrons aligning themselves for a while along the supplied alternating electric field. In low-frequency zones, polarization plays a key role in the high dielectric values. The lag in the time required to achieve polarization by electronic transferring over the charge carriers Fe^{2+} to Fe^{3+} can be utilized to explain the declining pattern of dielectric constant

with higher frequency. As the frequency of the externally applied field increases the electrons' frequency continues to hop because they are unable to quickly align with the alternating frequency of the field. Consequently, the decreasing movement of dielectric constant values in the high-frequency region is justified by the decreasing polarization magnitude. Figure. 22. Shows dielectric constant's effect on the composition of the sample can be used to directly explain the accessibility of iron ions on the octahedral regions. The higher value of the dielectric constant results from an increase in the polarization of the space charge whereas Mg^{2+} occupy A site which leads to an accumulation of Fe^{3+} ions on B sites. The smaller ionic size and low polarizability of Mg ions is the reason to increase accessibility of Fe^{3+}/ Fe^{2+} ions which may result from a decrease in dielectric constant with increasing concentration of Mg^{2+} that is shown in Figure. 22.

Table 5 Values of Dielectric constant (ε'), Dielectric loss (ε''). Tangent loss factor (δ), Ac conductivity (σAC), Real and imaginary part of impedance (Z') and imaginary part of impedance with respect to composition (x).

| Concentration	x=0.1	x=0.25	x=0.50	x=0.75	x=0.90
ε' (100Hz)	1280	1440	1180	4240	5750
ε'' (100Hz)	8197	7221	8225	2906	3572
tanδ (100Hz)	6.416	5.018	6.979	6.862	6.216
σ_{AC} at 100Hz (S-m$^{-1)}$	4.56×10^{-5}	4.01×10^{-5}	4.57×10^{-4}	1.62×10^{-3}	1.99×10^{-3}
ε' (1MHz)	8.23	9.13	1.23	2.04	2.85
ε'' (1MHz)	7.05	1.41	3.12	9.36	1.46
tanδ (1MHz)	0.335	0.466	0.732	1.168	1.263
σ_{AC} 1MHz (S-m$^{-1)}$	4.04×10^{-5}	8.09×10^{-5}	1.79×10^{-4}	5.36×10^{-4}	8.33×10^{-4}
Z' (100Hz)	1.02×10^{7}	1.87×10^{6}	7.41×10^{4}	2.06×10^{5}	2.54×10^{5}
Z'' (100Hz)	1.84×10^{6}	2.73×10^{5}	4.45×10^{5}	3.22×10^{4}	4.34×10^{4}
Z' (1MHz)	1.62×10^{6}	3.09×10^{3}	7.72×10^{3}	4.01×10^{3}	3.77×10^{3}
Z'' (1MHz)	2.00×10^{4}	1.93×10^{4}	9.23×10^{3}	7.92×10^{3}	7.35×10^{3}
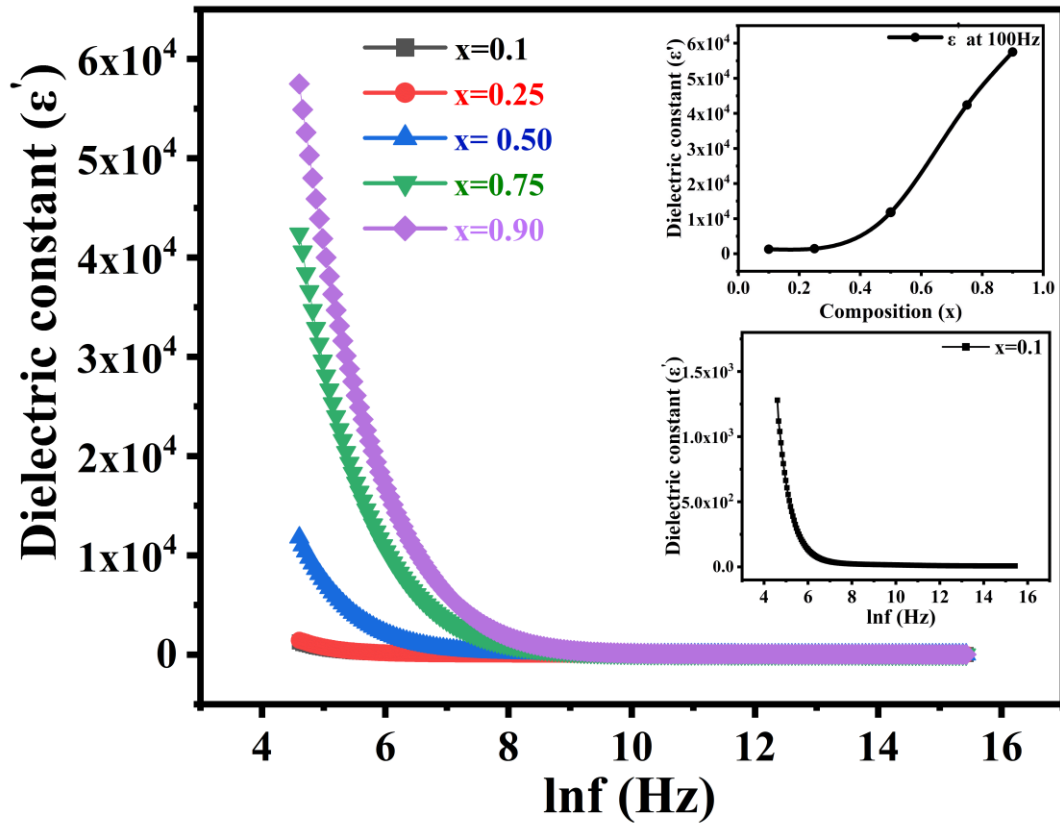
Figure 22 . Variability of the real part of Dielectric Constant (ε') against the logarithm of frequency of synthesized $Mg_xZn_{(1-x)}Fe_2O_4$ (x= 0.1, 0.25, 0.5, 0.75, 0.90) nanoparticles

4.1.4 Dielectric loss behaviour

The most important factor affecting the entire core loss in a ferrite system is the dielectric loss ε'' that is ability to determine the amount of heat dissipating inside a dielectric medium, defined as the imaginary component of the dielectric constant. The behaviour of the ε'' as a function of frequency is seen in Figure. 23. The observed patterns exhibited a similar appearance to the dielectric constant, showing high values in the low frequency and practically uniform behaviour above a specified limiting value of increasing frequency. The low-frequency zones are predicted by Koop's concept to represent the predominance of very resistant grain boundaries, this means that a lot of energy is required to transport the electrons from the charge carriers Fe^{2+} to Fe^{3+}. Furthermore, the low-frequency regions' hopping electrons follow the supplied

alternating field. The applied field frequency is significantly smaller than the frequency at which electron transit between charge carriers Fe^{2+} to Fe^{3+}. Such hopping is still being affected by the delayed polarization that comes from impurities, porosity, and other crystal defects. These defects serve as an insulating barrier, delaying the influence polarization at the expense of further energy. The combined effect of all the previous variables leads to the resistive grain boundary influence at low-frequency region. Therefore, ε'' has significant at low-frequency zones. Besides, it is becoming more common to observe a declining trend in dielectric loss. This may be accounted that the electrons' failure to adapt to the rapidly varying field by leaping more slowly between hop locations while applied alternating field frequency is substantially higher than the leaping frequency of the electrons [36], which explains the reason they don't jump as often. As a result, areas with high frequencies are dominated by grains with low conductivity. The gradual decline of ε'' of the high-frequency values which indicates that electron hopping often requires very low energy [38].
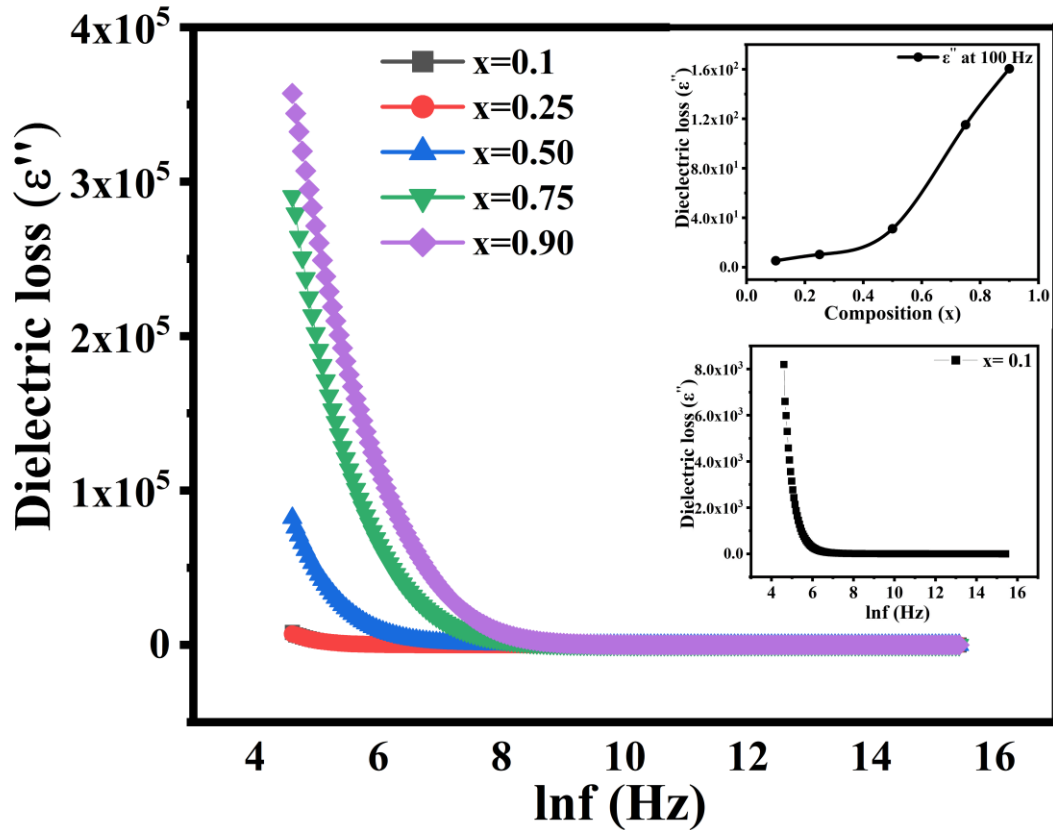
Figure 23 Variability of the real part of the Dielectric loss (ε'') variability against the logarithm of frequency of synthesized $Mg_xZn_{(1-x)}Fe_2O_4$ (x= 0.1, 0.25, 0.5, 0.75, 0.90) nanoparticles

4.1.5 Tangent loss behaviour

The energy loss in dielectric materials is represented as dielectric tanδ. Figure. 24. displays room temperature fluctuation from 100 Hz to 5 MHz. It's been found that the dielectric loss tangent exhibits a decreasing behaviour with the frequency at which an AC field is being used. When an alternating field is present, instead of being 90 times longer than the current flowing, the period required for polarization exhibits phase delay. The equation has been significantly progressed due to 90- δ, here δ represents the difference in phase between the applied alternating field and the induced current. This is the equation tanδ=1/2πfC$_p$R$_p$ that provides the complex plane's tangent to the phase variance [37]. Two different intrinsic mechanisms present in the ferrite matrix can be used to explain this phase difference, polarization dipole which reveals that polarization dipoles has slower responses with the supplied alternating field and lower frequency regions of the tanδ are dominated by electron hopping [38]. Although tanδ

represents a fundamental loss of electromagnetic energy, it is possible to link the delay between these two mechanisms. The fluctuation of tanδ is plotted against frequency, and the maximum values of dispersion occur for the sample x=0.9 and x=0.25 sample indicating minimum dispersion which can be displayed in Figure. 24. Additionally, dispersion tendency with increasing magnesium substitution is also observed in the insert. As was previously explained, simultaneously grains and grain boundaries have large resistance outcomes at low-frequency area therefore, electron hopping requires a lot of electrical energy.

The existence of crystal defects also causes more energy lost. This mean, due to the delayed response between polarization dipole orientations with relative to the alternating field orientation and increased use of energy, the initially higher tanδ values are acceptable. A large dielectric resonance peak for x=0.75 is observed, showing a relaxing time distribution rather than a singular relaxation time. Since it involves much fewer electrons hop and less amount of energy used in high-frequency area, the resistivity of grains reduces, suggesting that a decrease in tanδ is appropriate for high-frequency values. When the equation $\omega\tau=1$ achieved, where τ is the relaxation period and $\omega=2\pi f_{max}$ such a maximum can only be obtained in a dielectric substance [39] . The Debye relaxation model is frequently used to explain this observed discrepancy. This model predicts that such a peaked phenomenon will occur when the jumping electrons' hopping frequency coincides with the applied field frequency, resulting in a sharp increase in dielectric loss and the highest amount of electrical energy transferred. Moreover, Figure. 24. Shown the arbitrary values of tanδ that vary with magnesium substitution.

Multiple factors and their interactions such as Fe^{2+} production while compositional homogeneity and fluctuation, chemical uniformity, crystal structure, porosity percentage, and sintering have a long-lasting impact on the tangent loss factor. These variables are challenging to manage, and their influence changes as sintering temperature and compositional substitutions vary. As a result, variations in trends frequently arise and have been frequently reported[40, 41]. The structural homogeneity of the manufactured nanoparticles is also responsible for the general decrease in tanδ values that can be seen. Due to their exceptional magnetic and electrical properties, these dielectric materials with increasing magnesium concentrations are used in high-frequency applications.
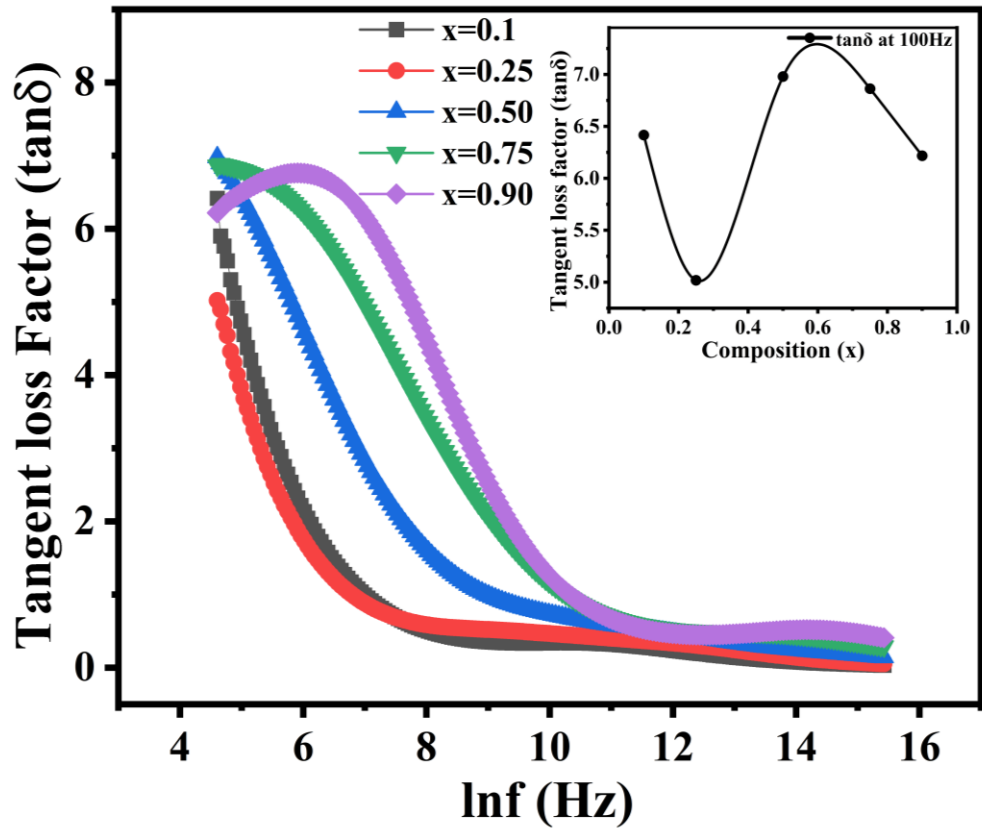
Figure 24 Tangent loss factor variability against the logarithm of frequency of synthesized Mgx Zn(1-x)Fe2O4 (x= 0.1, 0.25, 0.5, 0.75, 0.90) nanoparticles

4.1.6 Ac Conductivity behaviour

Figure. 25. shows the Ac conductivity as a function of frequency from 100 Hz to 5 MHz for magnesium-substituted zinc ferrite nanoparticles. The general relation given below expresses the relationship between the AC conductivity ($ϭ_{ac}$) and its frequency dependence [42].

$$ϭ_{total}(\omega) = ϭ_{dc}(T) + ϭ_{ac}(\omega,T) = ϭ_{dc}(T) + B\omega^n \qquad \text{.....(18)}$$

where the frequency-independent DC conductivity contribution of the conduction band is denoted by $ϭ_{dc}(T)$, $ϭ_{ac}(\omega,T)$ is defined as the frequency-dependent pure AC conductivity contribution of the electron hopping at the B sites. n stands for temperature-dependent frequency component, while B is the conductivity-related pre-exponential constant and $\omega = 2πf$ is the angular frequency

it is possible to see linear behavior to the dielectric constant, for instance, that low ac conductivity increases with frequency. It has been also found that conductivity increases as the concentration of Mg^{2+} increases. Fig. 8. shows the variation of ac conductivity at various concentrations of Mg^{2+}. This could be a result of electron and hole hopping [43]. The following is the proposed general process for ac conduction via electron and hole hopping [44]:

$$Fe^{3+} \leftrightarrow Fe^{2+} + e^{-} \qquad\qquad .....(19)$$

During the sintering process, Fe^{3+} and Fe^{2+} ions are released. These ions cause ac conduction by allowing electrons and holes to move between nearby B sites ($Fe^{3+} \leftrightarrow Fe^{2+}$). Following Koop's concept, grain boundaries act in a way that reduces charge carrier hopping for low frequencies. As a result, ac conductivity values at low-frequency areas seem to be constant. The greater hopping between charge carriers is caused by the presence of more conductive grains in higher-frequency areas which leads to an increase in ac conductivity with frequency. Fig. 8. shows another certainty is that ac conductivity also depends on the composition which is accounted for by increasing the concentration of Mg^{2+} which increases the supply of charge carriers at B sites and causes conduction.
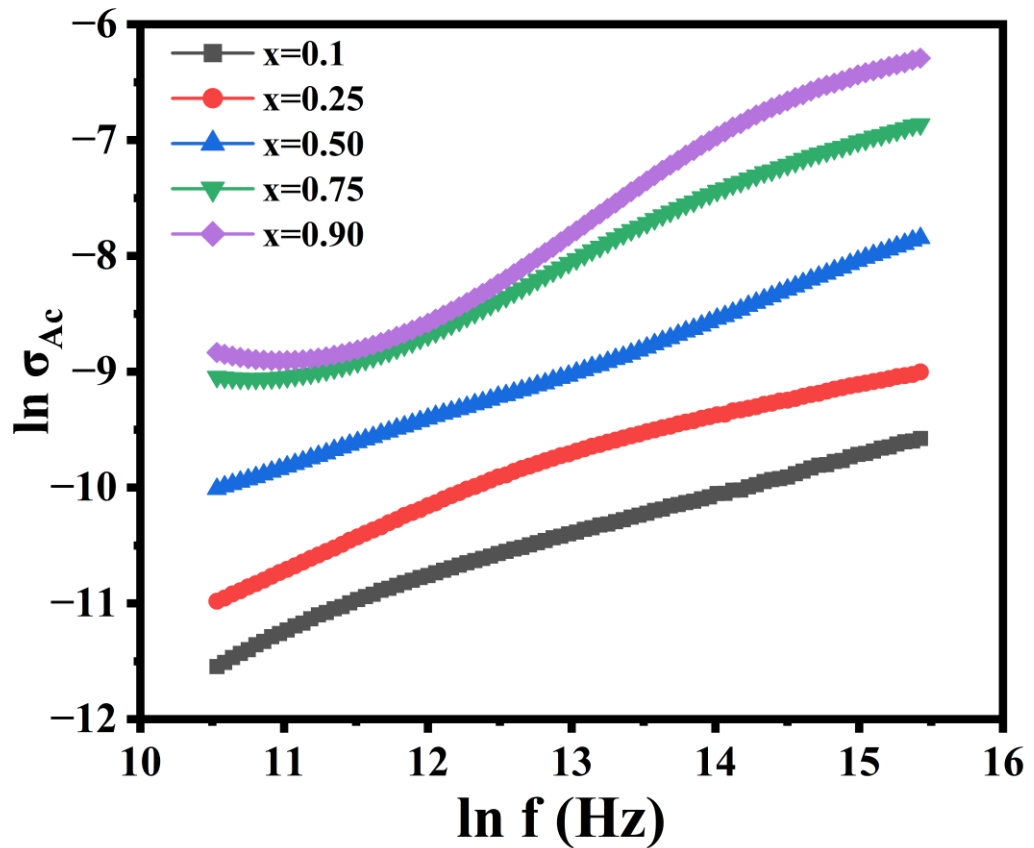
Figure 25 AC-Conductivity fluctuation for synthesized Mgx Zn(1-x)Fe2O4 (x= 0.1, 0.25, 0.5, 0.75, 0.90) nanoparticles as a function of frequency

4.1.7 Impedance Spectroscopy

Bauerle [43] became the initial researcher that used impedance spectroscopy to examine the sample's impedance from a microstructural perspective i.e in a polycrystalline system, interfacial properties are separated from the bulk which is composed of several grains oriented differently resulting in a variety of effective zones determining the conductance, resistance and ultimately a range of polarization relaxation durations. Complex impedance plots are frequently used to gather an in-depth understanding of electrical characteristics involving the interaction between various elements (such as grain boundaries, electrolyte interfaces and electrodes), the dielectric response, resistance to voltage, and charge relaxing conduct, along with their combined resistance to a dielectric medium's ability to conduct current. The following equation can be used to represent the total impedance (Z).

$$Z = Z' + Z'' \qquad\qquad\qquad …..(20)$$

Z' here stands for the real portion of the impedance which is the resistance that allows electricity to flow across an electric circuit in the presence of an alternating electric field and Z" for the imaginary impedance which can be quantitatively measured as $\tan\delta$ and correlated with the sample's capacitance. In the light of relationship:

$$tan\delta = \frac{\varepsilon''}{\varepsilon'} \qquad\qquad .....(21)$$

Impedance spectroscopy is therefore an effective technique for studying the dielectric behaviour of a resistant complexity of a material in relation to frequency whereby its application and characteristics are influenced by its chemical makeup, structure, distribution of additives, and imperfections.

Figures 26(a), as well as 26(b), shows the real and imaginary impedance values obtained in impedance of all synthesized samples with respect to the applied frequency range at room temperature. It is apparent that Z' values exhibit behaviour that is frequency dependent, In the lower frequency range Z' values have a larger magnitude which steadily over time decreases with increasing frequency before getting superimposed at the high-frequency values. According to Figure 9(b), the materials exhibit greater Z″ values at lower frequencies compared to the actual component (Z′) and these values subsequently decrease rapidly with an increase in frequency, which is attributed to the conductivity of the ferrites. At higher frequencies, Z″ shows a frequency-independent behaviour with minimal constant values due to a decrease in polarization. The figures depicted in Figure 11 illustrate that Z' and Z" follow a comparable pattern to the dielectric characteristics of the materials. For each composition, the curves of impedance seem to converge at elevated frequencies, which suggests that low resistant grains remain the dominant contributing factor. However, at higher frequencies demonstrates a behavior that is independent of frequency with small constant values arising from a reduction in polarization. Furthermore, it is important to emphasize that the polarization induced by space charge only applies to materials that have been partitioned into grains and grain boundaries, as previously explained in studies. At elevated frequencies, the polarization of space charge decreases leading to the convergence of curves. This convergence validates the semiconducting characteristics of nanocrystalline spinel ferrites and explains the increased tendency for ac conductivity with frequency.

Nyquist plot (Z' vs Z'') is an additional method for assessing the response displayed on the plot is a combination of the resistor and capacitor in parallel, connected in an RC circuit. This plot helps to identify the contribution of grain and grain boundary resistance. Multiple electrical responses are observed in the synthesized material's heterostructure nature, along with the characteristic complex impedance spectra. These responses are due to the grain resistance Rg, grain boundary resistance Rgb, and electrode effects. The semicircular arcs that appear in the Nyquist plots make it easy to determine these effects. The complex impedance of real and imaginary component curves for each composition is shown in Figure. 26(c) which exhibit non-Debye type relaxation behaviour due to their asymmetrical shapes carrying imperfections or defects. The size of the semicircular arcs that make up the diameter has been observed to decrease as the concentration of Mg increases, which is due to the resistance of the grain boundaries. Nonetheless, at lower frequencies, the appearance of the first semicircle is primarily governed by Rg, while the appearance of the second semicircle is mainly influenced by Rgb at higher frequencies. The primary driving force behind the separation of the semicircular arcs is believed to be the difference in relaxation time.
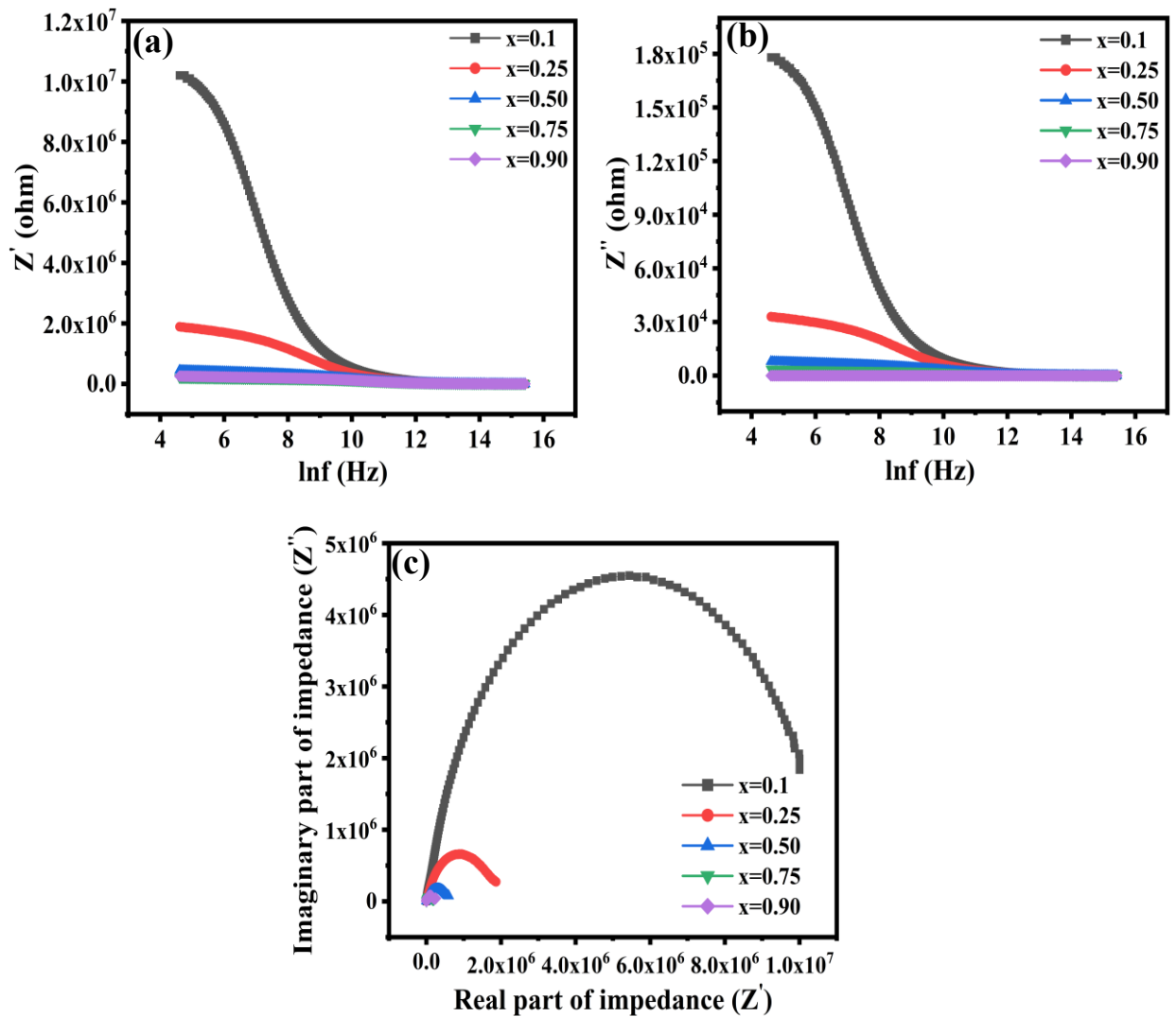
Figure 26 Variation of real part of impedance (Z′), (b) imaginary part of impedance (Z″) as a function of logarithm of frequency and (c) Nyquist plot of Z′ vs Z″ of impedance for synthesized Mgx Zn(1-x)Fe2O4 (x= 0.1, 0.25, 0.5, 0.75, 0.90) nanoparticles

4.1.8 EMI shielding.

Electromagnetic Shielding (EMI) measurement is used to assess the ability of materials to block or reduce the transmission of electromagnetic radiation. In electronic systems, EMI can cause interference, malfunction, or damage, which highlights the importance of measuring the shielding effectiveness of materials. To evaluate the shielding effectiveness of a material, it is necessary to obtain the transmittance (T), reflectance (R), and absorbance (A) of the material. The electromagnetic shielding potential of the samples was studied in the frequency range of (0–3 GHz). The EMI SE refers to the decrease in electromagnetic interference within certain frequency ranges, which is

determined by the ratio of transmitted power (Pt) to incident power (Pi). This ratio is typically expressed in decibels (dB) and can be defined using the below eequation (22).

$$SE_{total}(dB) = -10\log\left(\frac{Pt}{Pi}\right) \qquad .....(22)$$

Higher values of SE_{total} refer to effective absorption or reflection of large number of radiations much higher than the transmission [45]. The complete shielding efficiency (or overall loss) is the combination of the effects from reflection (SE_R), absorption (SE_A), and multiple reflections (SE_M), and is referred to as the total shielding effectiveness (SE_{total}) that is given in below eequation (23) according to references [45, 46].

$$SE_{total}(dB) = SE_A + SE_R + SE_M \qquad .....(23)$$

When SE_A is greater than 10 dB, SE_M can be ignored, and SE total now will be written as:

$$SE_{total}(dB) = SE_A + SE_R \qquad .....(24)$$

The measurement of transmittance (T), reflectance (R), and absorbance (A) through the shielding material is done by using scattering parameters (S11 or (S22) and S12 or (S21)), which corresponds to reflection and transmission coefficients, respectively [47, 48].

$$T = S_{12}^2 = S_{21}^2 \qquad .....(25)$$
$$R = S_{11}^2 = S_{22}^2 \qquad ..... (26)$$
$$A = 1 - R - T \qquad ..... (27)$$

A is determined based on the power of the incident electromagnetic wave. When there are no multiple reflections, the absorbance can be effectively defined as Á, with respect to the power of the incident electromagnetic wave inside the shielding material, using Eq. (7)[49].

$$Á = (1 - R - T) / (1 - R)$$
$$.....(28)$$

The overall EMI SE can also be achieved as in below equation from the direct calculated S-parameters[49].

$$SE = 10\log\frac{1}{|S_{12}|^2} = 10\log\frac{1}{|S_{21}|^2} \qquad .....(29)$$

Figure. 27. shows frequency dependent EMI SE (dB) for the synthesized $Mg_x Zn_{(1-x)}$ Fe_2O_4 (x= 0.1, 0.25, 0.5, 0.75, 0.90) nanoparticles in S- band where the effect of Mg substitution in the ferrite sample on the SE is evident. When magnesium substitution is increased, the effectiveness of EMI shielding absorption is also increased to -27.3 dB at 2.9 GHz, and the reflection loss decreases to -9.7 dB at 0.15 GHz. These changes are attributed to the dielectric properties which are explain in the previous section. SE_T values are overall increase upto -33.7 dB at 3 GHz
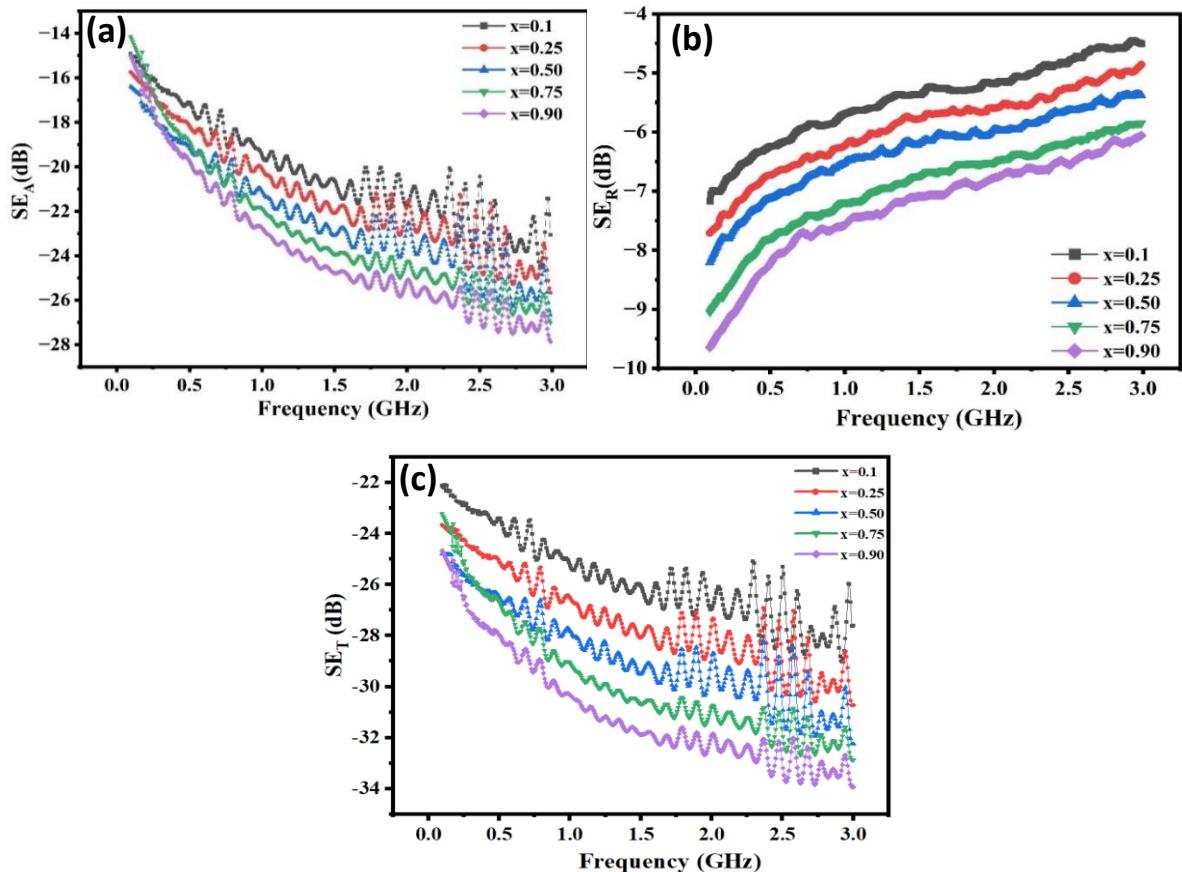

Figure 27 Frequency dependent graphs of (a) refection loss (b) absorption (c) total of synthesized $Mg_xZn_{(1-x)}Fe_2O_4$ (x= 0.1, 0.25, 0.5, 0.75, 0.90) nanoparticles

4.2 Part-2 Aluminum incorporated Mg-Zn ferrite for Emi shielding.

4.2.1 Background

In the previous section five compositions of Mg-Zn ferrite were synthesized in $[Mg_xZn_{(1-x)}Fe_2O_4]$ (x= 0.1,0.25, 0.50, 0.75, 0.90) through solgel method. Composition x=0.90 showed better dielectric and EMI shielding properties among other compositions so nanoparticles of aluminum were added in different percentage utilizing

the $Al_x/Mg_xZn_{(1-x)}Fe_2O_4$ formula, (x= 0.1%, 0.5%, and 1%) to this composition via ball milling. To achieve better shielding properties

incorporation of aluminum in Mg-Zn ferrite was investigated through various characterizations. For the purpose of electrical testing, a sandwich pellet consisting of three layers has been created. The upper layer is made of pure ferrite with an optimal composition of 0.9, while the middle layer incorporates aluminum ferrite. The lower layer is made of pure ferrite and can be viewed in the accompanying figure.

4.2.2 XRD

X-ray diffraction (XRD) was utilized to investigate the structural characteristics of aluminium-incorporated Mg-Zn ferrites at varying concentrations. The XRD patterns for both Mg-Zn ferrites for (x=0.9) and the $Al_x/Mg_xZn_{(1-x)}Fe_2O_4$ matrix with distinct stoichiometric levels of aluminium (x = 0.1% , 0.5% , 1%), are illustrated in Figure 28. The X-ray diffraction (XRD) patterns of Mg–Zn Fe_2O_4 exhibited several peaks that were identified as (220), (311), (400), (422), (511), (440), and (533) of the cubic crystal structure of mixed spinel ferrites. This is in agreement with the JCPDS card number (01-086-1345), thereby confirming the presence of such a structure. The synthesized samples do not present any supplementary peak that confirms their purity, although the main peak along the plane (311) is both sharp and fine, thereby indicating a successful crystallization process. Additionally, the absence of any supplementary peak can also be attributed to the fact that Al is distributed throughout the entirety of the synthesized ferrite. due to this reason the lack of observable aluminium peaks can be attributed to the low concentration of Al present in the samples. Notably, the XRD scanning time was relatively brief.
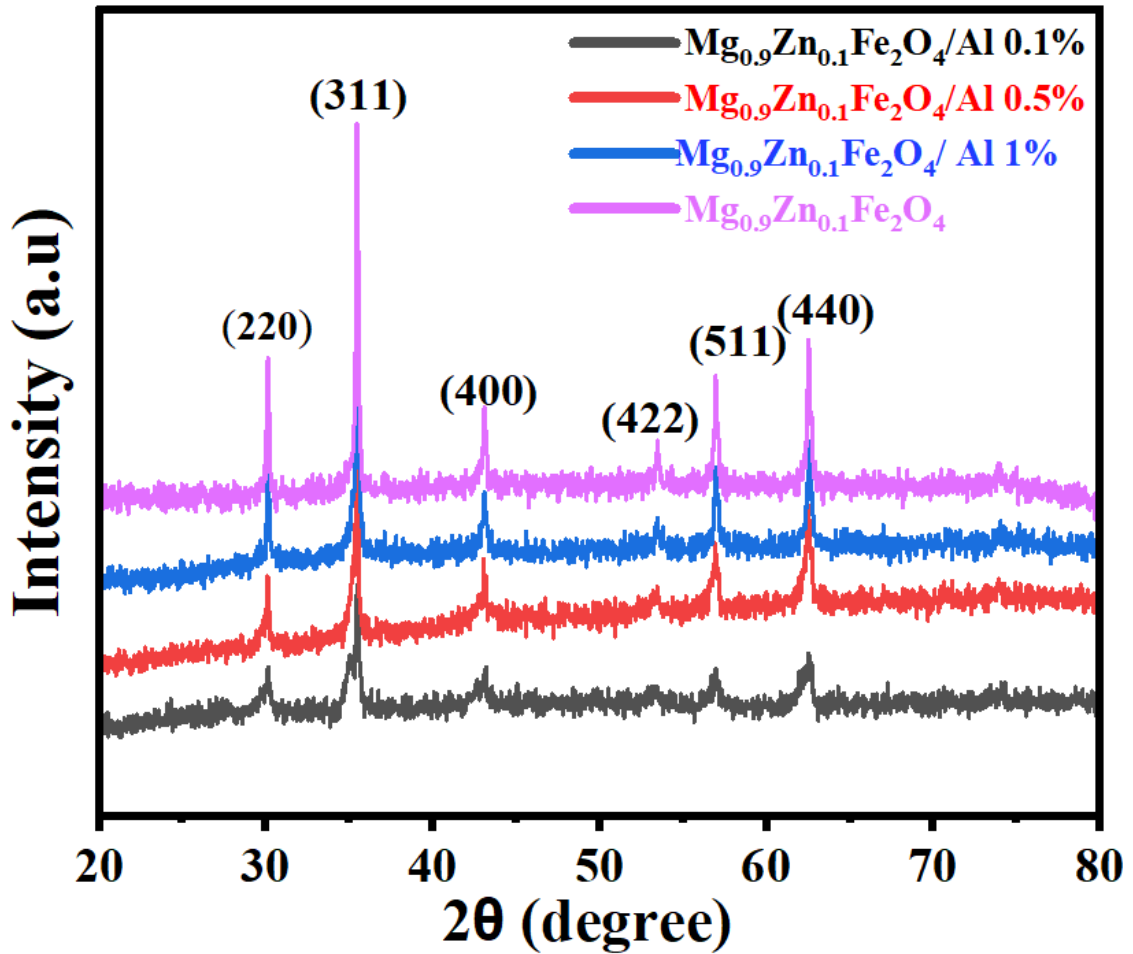
Figure 28 XRD spectrum for $Al_x/Mg_{0.9}Zn_{0.1}Fe_2O_4$ (x= 0.1%, 0.5%, 1%) samples.

4.2.3 Dielectric properties

Figure. 29. Highlights the impact of Al nanoparticles on the dielectric constant of Mg-Zn ferrite. The real part of dielectric constant (ε') might be explained by the predominance of space charge polarization resulting from the heterogeneous dielectric system in ferrites. Figure.29. shows the variance of real part of dielectric constant (ε') in relation to the frequency range from 100Hz to 5MHz of the applying electric field. The high dielectric constant values of all manufactured samples at low frequencies and decline at higher frequencies. With the help of Koop's concept [18 al] which states that ferrite material is composed of grain and grain boundaries, where the resistance of grain boundaries in ferrite material is higher than resistance of grains [50, 51]. when a low-frequency electric field is applied charges assembles at the grain boundaries' interfaces. these charges assist in creating polarization. It explains the high dielectric values (ε') at low frequencies. However, the potential reason of the decrease in dielectric constant at high frequencies could be a reduction in interfacial polarization due to majority of

charge carriers being unable to follow sharp fluctuations of the applied electric field at higher frequencies. In ferrites, Rabinkin and Novikova [51] state that polarization is explained due to the localized migration of electrons through ionic interaction of Fe^{2+} and Fe^{3+} ions in the direction of the applied field. Besides this, the increased dielectric constant at a low frequency in Mg-Zn ferrite is attributed to the domination of Fe^{2+} ions and oxygen vacancies [36]. Although, the ionic interaction of ions unable to align with the changing field frequency at high frequency [51]. Figure. 29. clearly depicts with the addition of Al nanoparticles, $Al/Mg-ZnFe_2O_4$ was shown to have a higher dielectric constant than $Mg-ZnFe_2O_4$ between middle and low frequencies. At lower frequency, 1% of Al in $Al/Mg-ZnFe_2O_4$ yielded the maximum dielectric constant in the range of (10^5). Due to uniform aluminum nanoparticle distribution on the grains of $Mg-ZnFe_2O_4$, 0.5% of Al in $Al/Mg-ZnFe_2O_4$ represented the much more stable and highest dielectric constant behavior with regards to frequency. The $Mg-ZnFe_2O_4$ system has aluminum metal particles, which enables to generate the micro or nanocapacitors and enhances the dielectric constant.
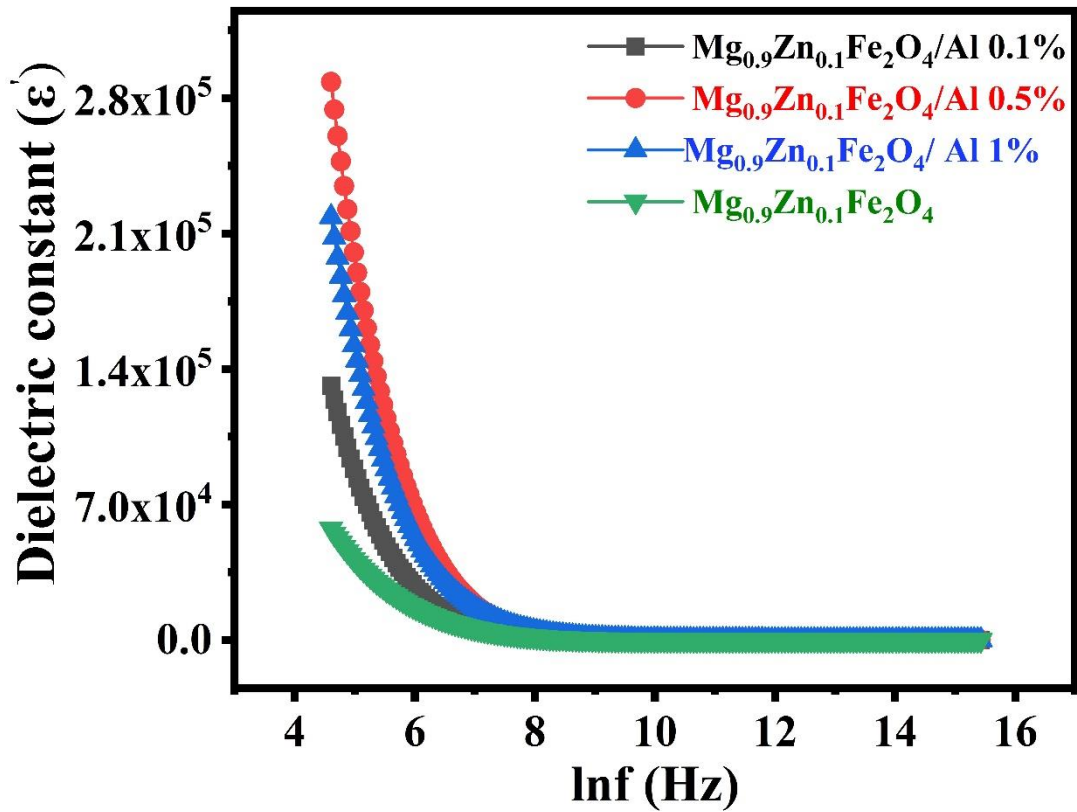
Figure 29 . Variance in the dielectric constant (ε') of $Al_x/Mg_{0.9}Zn_{0.1}Fe_2O_4$ samples having composition (0 .1%, 0.5% 1%) with frequency.

Figure. 30. Represent the findings of a study on the variability of tangent loss (tanδ) as a function of frequency. Tangent loss exhibited a frequency-dependent declining tendency in all samples. The distinction in tangent loss across all samples can be attributed to the transition of space charge carriers trapped at grain boundaries with an increase in applied field frequency [36]. All $Al/Mg\text{-}ZnFe_2O_4$ matrix clearly shows a significant peak around 8.5 and 14 kHz, but it seems that the tangent loss curve of $Mg\text{-}ZnFe_2O_4$ had a minor hump at about 6.3 kHz. In Ferrites the dielectric properties are integrally linked to their conduction process, which is the ionic interaction of Fe^{2+} to Fe^{2+} ions towards octahedral site. Figure. 30. depicts the highest tangent loss due to the external electric field frequency and the electronic exchange frequency are in phase. Furthermore, by Comparing the $Mg\text{-}ZnFe_2O_4$ to $Al/Mg\text{-}ZnFe_2O_4$ matrix it has been observed that excess amount of charge carriers is participating in polarization which leads to enhanced dielectric characteristics of $Al/Mg\text{-}ZnFe_2O_4$ matrix. Fig.4. exhibited the highest tangent loss in $Al_x/Mg_x\text{-}Zn_{1-x}Fe_2O_4$ for (x=0.5%).
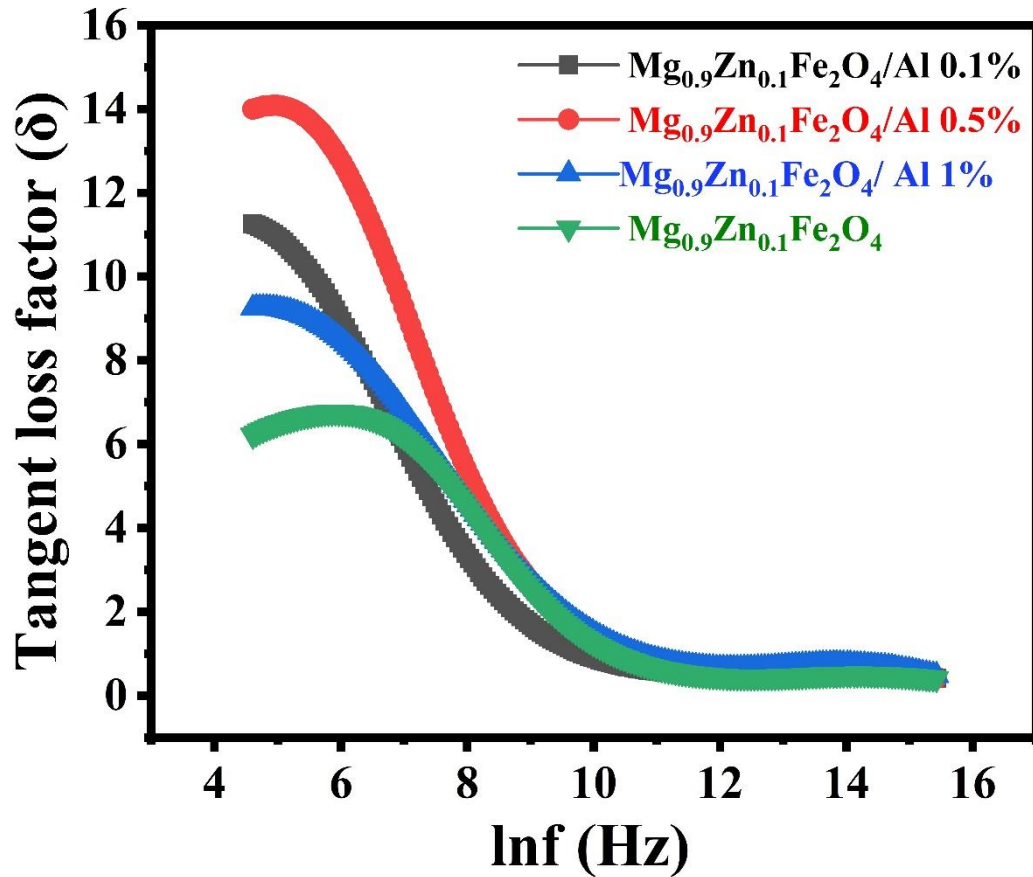
Figure 30 Variance in the tangent loss (δ) of $Al_x/Mg_{0.9}Zn_{0.1}Fe_2O_4$ having composition (0 .1%, 0.5% 1%) with frequency.

4.9.3 EMI shielding

The EMI shielding Network Analyzer utilized the coaxial cable method to measure shielding effectiveness, with a maximum range of -38 dB. To conduct this measurement, a donut-shaped sample was fabricated with a thickness of 0.25 mm, an outer diameter of 7 mm, and an inner diameter of 3 mm. Shielding effectiveness is determined by the logarithmic ratio of incoming and transmitted EM wave energy.

$$SE_{total}(dB) = -10 \log\left(\frac{Pt}{Pi}\right)$$ .....(30)

The VNA was used to obtain the scattering parameters or S-parameters (S11, S12, S21, and S22)[52], which were then plugged into equations to determine shielding effectiveness through reflection (SER), absorption (SEA), and total shielding effectiveness (SET).

The SET is calculated as the sum of the SER and SEA.

$$SE_{total}(dB) = SE_A + SE_R$$

$$\ldots\ldots(31)$$

The formulas for SEA and SER are expressed as logarithmic equations (32),(33) [53]with the results for all three types of shielding effectiveness shown in Figure. 31.

$$SE_A = 10\log\frac{1-|S_{11}|^2}{|S_{21}|^2} \qquad \ldots\ldots(32)$$

$$SE_R = 10\log\frac{1}{|S_{11}|^2} \qquad \ldots\ldots(33)$$

Figure 32(a) demonstrates that samples containing $Mg_{0.9}Zn_{0.1}Fe_2O_4$ ferrite showed absorption of -25.2 dB at 2.9 GHz in higher frequency and -14.5 dB at 0.14 GHz in lower frequency and maximum absorption of -30 dB at 3 GHz in higher frequency and -20.5 dB at 0.14 GHz in lower frequency for sample $Al_{0.5}/Mg_{0.9}Zn_{0.1}Fe_2O_4$ in S band. Samples including Al exhibit improved absorption as composition is gradually increased. The high absorption in the ferrite matrix was due to the aluminium particles dispersed within it. Mg-Zn spinel ferrites possess magnetic domains and serve as absorbing sites for EM wave, resulting in high SEA values. A sample of $Mg_{0.9}Zn_{0.1}Fe_2O_4$ ferrite displays reflection of -6.3 dB at 2.9 GHz in higher frequency and -9.6 at 0.13 GHz at lower frequency. Additionally, the maximum reflection is -8.4 dB at 3 GHz in higher frequency and -9.9 at 0.12 GHz at lower frequency for sample $Al_{0.5}/Mg_{0.9}Zn_{0.1}Fe_2O_4$. However, sample with an $Al_{0.5}/Mg_{0.9}Zn_{0.1}Fe_2O_4$ ferrite matrix showed very low SER values than SEAdue to the matrix's low electrical conductivity and non-conductive surface caused by pure ferrite. The shielding effectiveness values exhibited an increase, with a maximum of -38 dB at 3 GHz for $Al_{0.5}/Mg_{0.9}Zn_{0.1}Fe_2O_4$. As per the theory of EMI shielding, when an EM wave falls on an electrically conductive surface, it reflects back, while it gets absorbed when it falls on a magnetic surface. aluminum particles are distributed throughout the Mg-Zn ferrite system, with the outer surface being mostly non-conductive. The SER is not particularly high, indicating that the majority of the electromagnetic wave has penetrated the shielding material. Once the EM wave has entered the shield, the electrically conductive interfaces of aluminum and the magnetic interfaces of Mg-Zn

ferrite reflect and absorb the EM wave through several reflections within the material, as depicted in Figure 31.
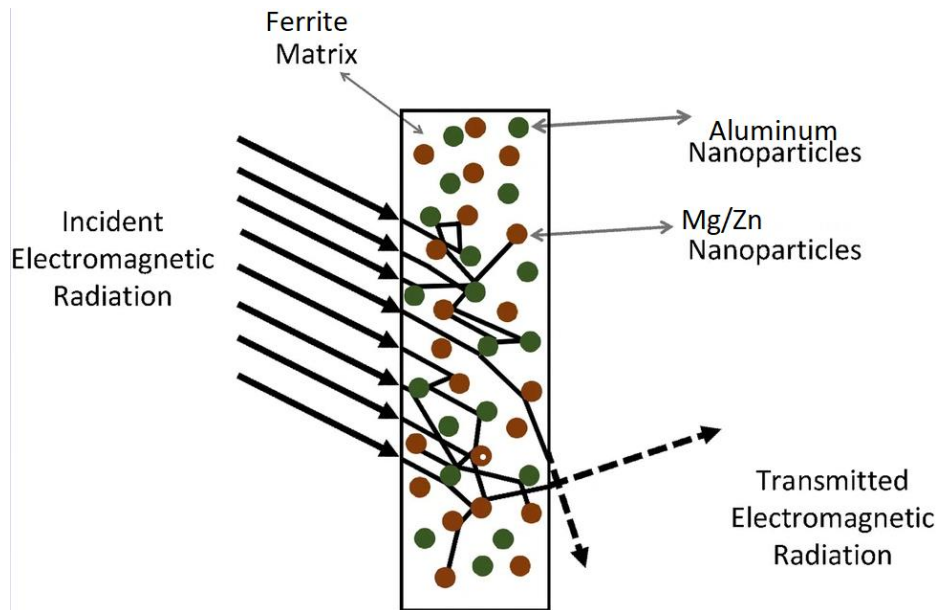

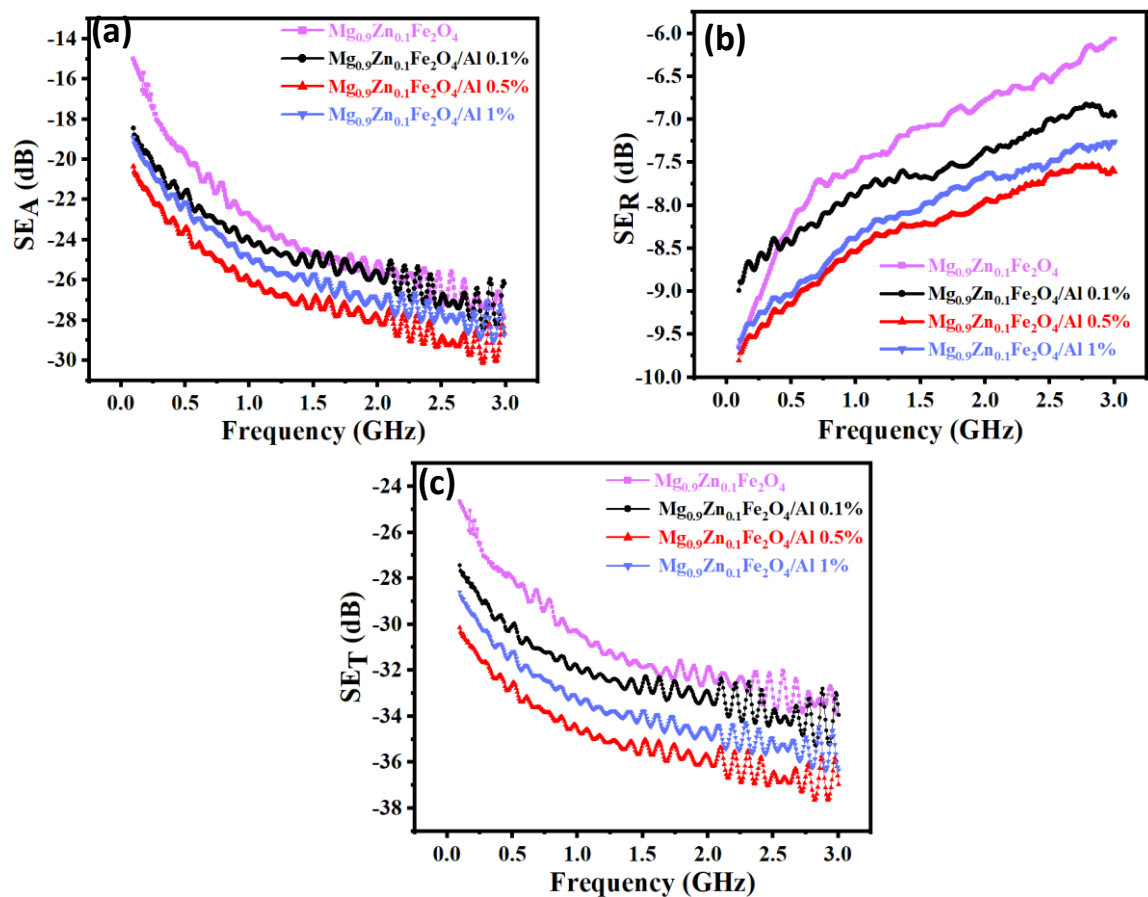**Figure 31** Electromagnetic wave diagram for the Al/Mg-Zn ferrite system

Figure 32 EMI graph of (a) absorption, (b) reflection (c) Transmission of $Al_x/Mg_{0.9}Zn_{0.1}Fe_2O_4$ having composition (0 .1%, 0.5% 1%)

Conclusion

Mg substituted Zn ferrite nanoparticles ($Mg_xZn_{1-x}Fe_2O_4$ x=0.1, 0.2, 0.5, 0.75, and 0.90) were synthesized by using the fast and effective sol-gel combustion method. The effect of various concentrations of Mg was comprehensively investigated through advanced characterization techniques like XRD, SEM, FTIR, VSM, IA, VNA on the structural, morphological, electrical and EMI properties of all samples. XRD characterization of cubic spinel phase which confirms the decreased crystallite size with increase in the concentration of Mg for all samples. Lattice constant was also found to be decreased from 8.43 Å to 8.40 Å. FTIR spectra showed two significant absorption band exhibiting intrinsic stretching vibration of O_2-Fe_3 approximately (551 to 566 cm^{-1} v1 and 424 cm^{-1} to 439 cm^{-1}) that represent the spinel structure. Dielectric characteristics of the Mg-Zn Ferrite were analysed within the frequency range of 100 Hz to 5 kHz. The real and imaginary components of the dielectric constant were found to rise in direct proportion to the magnesium content. Frequency dependent dielectric constant of each samples exhibit an overall tendency towards attaining the largest values in the zone of low-frequency and declining with a rising frequency zone eventually it almost stops changing after a specific high-frequency value. EMI results are in well agreement with dielectric properties sample having 0.9 composition showed enhanced absorption and low reflection loss with increasing concentration of Mg. Addition of Al nanoparticles in Mg-Zn ferrite matrix further improved dielectric properties and EMI results. 0.5 Al/Mg–ZnFe2O4 showed more stable dielectric properties with frequency and EMI results is going to decrease for the reflection loss SER= -9.9 dB at 0.15GHz and absorption performance is enhanced with SEA= -37.8 dB at 3 GHz EMI properties of Al incorporated Mg-Zn ferrite system highlights the potential to shield material for electronics applications.

References

[1] Xing, D., Lu, L., Xie, Y., Tang, Y., & Teh, K. S. (2020). Highly flexible and ultra-thin carbon-fabric/Ag/waterborne polyurethane film for ultra-efficient EMI shielding. *Materials & Design*, *185*, 108227.

[2] Song, Q., Ye, F., Yin, X., Li, W., Li, H., Liu, Y., ... & Wei, B. (2017). Carbon nanotube–multilayered graphene edge plane core–shell hybrid foams for ultrahigh-performance electromagnetic-interference shielding. *Advanced Materials*, *29*(31), 1701583.

[3] Martirosyan, K. S., Galstyan, E., Hossain, S. M., Wang, Y. J., & Litvinov, D. (2011). Barium hexaferrite nanoparticles: synthesis and magnetic properties. *Materials Science and Engineering: B*, *176*(1), 8-13.

[4] Wilson, R., George, G., & Joseph, K. (2020). An introduction to materials for potential EMI shielding applications: Status and future. In *Materials for Potential EMI Shielding Applications* (pp. 1-8). Elsevier.

[5] Alam, R. S., Moradi, M., Rostami, M., Nikmanesh, H., Moayedi, R., & Bai, Y. (2015). Structural, magnetic and microwave absorption properties of doped Ba-hexaferrite nanoparticles synthesized by co-precipitation method. *Journal of Magnetism and Magnetic Materials*, *381*, 1-9.

[6] Rahaman, M., Chaki, T. K., & Khastgir, D. (2011). High-performance EMI shielding materials based on short carbon fiber-filled ethylene vinyl acetate copolymer, acrylonitrile butadiene copolymer, and their blends. *Polymer composites*, *32*(11), 1790-1805.

[7] Channe, S. S., Singh, R., & Kulkarni, S. G. (2023). Effect of metal oxide nanoparticles on thermal behavior of polyvinyl alcohol. *Polymer Bulletin*, 1-36.

[8] Pratap, V., Soni, A. K., Dayal, S., Abbas, S. M., Siddiqui, A. M., & Prasad, N. E. (2018). Electromagnetic and absorption properties of U-type barium hexaferrite-epoxy composites. *Journal of Magnetism and Magnetic Materials*, *465*, 540-545.

[9] Dijith, K. S., Aiswarya, R., Praveen, M., Pillai, S., & Surendran, K. P. (2018). Polyol derived Ni and NiFe alloys for effective shielding of electromagnetic interference. *Materials Chemistry Frontiers*, *2*(10), 1829-1841.

[10] Ji, K., Zhao, H., Zhang, J., Chen, J., & Dai, Z. (2014). Fabrication and electromagnetic interference shielding performance of open-cell foam of a Cu–Ni alloy integrated with CNTs. *Applied Surface Science*, *311*, 351-356.

[11] Rana, K., Thakur, P., Tomar, M., Gupta, V., & Thakur, A. (2018). Investigation of cobalt substituted M-type barium ferrite synthesized via co-precipitation method for radar absorbing material in Ku-band (12–18 GHz). *Ceramics International*, *44*(6), 6370-6375.

[12]   Li, W., Qiao, X., Li, M., Liu, T., & Peng, H. X. (2013). La and Co substituted M-type barium ferrites processed by sol–gel combustion synthesis. *Materials Research Bulletin*, *48*(11), 4449-4453.

[13]   Abbas, S., & Anis-ur-Rehman, M. (2016). Association of structural and enhanced transport properties in RE substituted cobalt nanoferrites. *Journal of Alloys and Compounds*, *677*, 143-147.

[14]   Pendyala, S. K., Thyagarajan, K., GuruSampath Kumar, A., & Obulapathi, L. (2018). Effect of Mg doping on physical properties of Zn ferrite nanoparticles. *Journal of the Australian Ceramic Society*, *54*, 467-473.

[15]   Zhao, J., Wang, T., Liu, X., Kan, X., Liu, C., Wang, W., ... & Shazeda, M. (2021). Influence of Mg 2+ replacement on the structure and magnetic properties of Mg x Zn 1− x Fe 2 O 4 (x= 0.1–0.5) ferrites. *Journal of Materials Science: Materials in Electronics*, *32*, 4008-4020.

[16]   Li, F., Liu, J., Evans, D. G., & Duan, X. (2004). Stoichiometric synthesis of pure MFe2O4 (M= Mg, Co, and Ni) spinel ferrites from tailored layered double hydroxide (hydrotalcite-like) precursors. *Chemistry of materials*, *16*(8), 1597-1602.

[17]   Hajalilou, A., & Mazlan, S. A. (2016). A review on preparation techniques for synthesis of nanocrystalline soft magnetic ferrites and investigation on the effects of microstructure features on magnetic properties. *Applied Physics A*, *122*, 1-15.

[18]   Racero, F. J., Bueno, S., & Gallego, M. D. (2020). Predicting students' behavioral intention to use open source software: A combined view of the technology acceptance model and self-determination theory. *Applied Sciences*, *10*(8), 2711.

[19]   Skołyszewska, B., Tokarz, W., Przybylski, K., & Kakol, Z. (2003). Preparation and magnetic properties of MgZn and MnZn ferrites. *Physica C: Superconductivity*, *387*(1-2), 290-294.

[20]   Prakash, T., Williams, G. V., Kennedy, J., & Rubanov, S. (2016). Formation of magnetic nanoparticles by low energy dual implantation of Ni and Fe into SiO2. *Journal of Alloys and Compounds*, *667*, 255-261.

[21]   Kannan, Y. B., Saravanan, R., Srinivasan, N., & Ismail, I. (2017). Sintering effect on structural, magnetic and optical properties of Ni0. 5Zn0. 5Fe2O4 ferrite nano particles. *Journal of Magnetism and Magnetic Materials*, *423*, 217-225.

[22]   Jalaiah, K., & Babu, K. V. (2017). Structural, magnetic and electrical properties of nickel doped Mn-Zn spinel ferrite synthesized by sol-gel method. *Journal of Magnetism and Magnetic Materials*, *423*, 275-280.

[23]   Gul, I. H., Ahmed, W., & Maqsood, A. (2008). Electrical and magnetic characterization of nanocrystalline Ni–Zn ferrite synthesis by co-precipitation route. *Journal of magnetism and magnetic materials*, *320*(3-4), 270-275.

[24]   Vekas, L., Avdeev, M. V., & Bica, D. (2009). Magnetic nanofluids: synthesis and structure. *Nanoscience in biomedicine*, 650-728.

[25]   Tian, T., Scullion, D., Hughes, D., Li, L. H., Shih, C. J., Coleman, J., ... & Santos, E. J. (2019). Electronic polarizability as the fundamental variable in the dielectric properties of two-dimensional materials. *Nano letters*, *20*(2), 841-851.

[26]   Hossain, I., Islam, M. T., Samsuzzaman, M., Alsaif, H., Rmili, H., & Soliman, M. S. (2023). Dielectric characterization of Mg–Zn ferrite-based high permittivity flexible substrate for SNG metamaterial. *Journal of Materials Research and Technology*, *24*, 879-894.

[27]   Sharma, R., Thakur, P., Kumar, M., Barman, P. B., Sharma, P., & Sharma, V. (2017). Enhancement in AB super-exchange interaction with Mn2+ substitution in Mg-Zn ferrites as a heating source in hyperthermia applications. *Ceramics International*, *43*(16), 13661-13669.

[28]   Abdel-Aal, S. K., & Abdel-Rahman, A. S. (2020). Graphene influence on the structure, magnetic, and optical properties of rare-earth perovskite. *Journal of Nanoparticle Research*, *22*(9), 267.

[29]   Ahsan, M. Z., Islam, M. A., Bally, A. A., & Khan, F. A. (2020). Spectroscopic analysis for electric and magnetic properties of manganese doped cobalt nanoferrite. *Results in Physics*, *17*, 103172.

[30]   Reyes-Rodríguez, P. Y., Cortés-Hernández, D. A., Escobedo-Bocardo, J. C., Almanza-Robles, J. M., Sánchez-Fuentes, H. J., Jasso-Terán, A., ... & Hurtado-López, G. F. (2017). Structural and magnetic properties of Mg-Zn ferrites (Mg1− xZnxFe2O4) prepared by sol-gel method. *Journal of Magnetism and Magnetic Materials*, *427*, 268-271.

[31]   Waldron, R. D. (1955). Infrared spectra of ferrites. *Physical review*, *99*(6), 1727.

[32]   Shirsath, S. E., Toksha, B. G., Kadam, R. H., Patange, S. M., Mane, D. R., Jangam, G. S., & Ghasemi, A. (2010). Doping effect of Mn2+ on the magnetic behavior in Ni–Zn ferrite nanoparticles prepared by sol–gel auto-combustion. *Journal of Physics and Chemistry of Solids*, *71*(12), 1669-1675.

[33]   Raju, K., Balaji, C. G., & Reddy, P. V. (2014). Microwave properties of Al and Mn doped nickel ferrites at Ku band frequencies. *Journal of magnetism and magnetic materials*, *354*, 383-387.

[34] Maxwell, J. A. (2016). Expanding the history and range of mixed methods research. *Journal of mixed methods research*, *10*(1), 12-27.

[35] Yager, W. A. (1936). The distribution of relaxation times in typical dielectrics. *Physics*, *7*(12), 434-450.

[36] Kavasoglu, A. S., Kavasoglu, N., & Oktik, S. (2008). Simulation for capacitance correction from Nyquist plot of complex impedance–voltage characteristics. *Solid-state electronics*, *52*(6), 990-996.

[37] Hamdaoui, N., Azizian-Kalandaragh, Y., Khlifi, M., & Beji, L. (2019). Structural, magnetic and dielectric properties of Ni0. 6Mg0. 4Fe2O4 ferromagnetic ferrite prepared by sol gel method. *Ceramics International*, *45*(13), 16458-16465.

[38] Gul, I. H., & Pervaiz, E. (2012). Comparative study of NiFe2− xAlxO4 ferrite nanoparticles synthesized by chemical co-precipitation and sol–gel combustion techniques. *Materials research bulletin*, *47*(6), 1353-1361.

[39] Patange, S. M., Shirsath, S. E., Lohar, K. S., Jadhav, S. S., Kulkarni, N., & Jadhav, K. M. (2011). Electrical and switching properties of NiAlxFe2− xO4 ferrites synthesized by chemical method. *Physica B: Condensed Matter*, *406*(3), 663-668.

[40] Ajmal, M., Islam, M. U., Ashraf, G. A., Nazir, M. A., & Ghouri, M. I. (2017). The influence of Ga doping on structural magnetic and dielectric properties of NiCr0. 2Fe1. 8O4 spinel ferrite. *Physica B: Condensed Matter*, *526*, 149-154.

[41] Khan, M. Z., Gul, I. H., Anwar, H., Ameer, S., Khan, A. N., Khurram, A. A., ... & Mumtaz, M. (2017). Massive dielectric properties enhancement of MWCNTs/CoFe2O4 nanohybrid for super capacitor applications. *Journal of Magnetism and Magnetic Materials*, *424*, 382-387.

[42] Mazen, S. A., & Abu-Elsaad, N. I. (2017). Dielectric properties and impedance analysis of polycrystalline Li-Si ferrite prepared by high energy ball milling technique. *Journal of Magnetism and Magnetic Materials*, *442*, 72-79.

[43] Bauerle, J. E. (1969). Study of solid electrolyte polarization by a complex admittance method. *Journal of Physics and Chemistry of Solids*, *30*(12), 2657-2670.

[44] Hashim, M., Kumar, S., Ali, S., Koo, B. H., Chung, H., & Kumar, R. (2012). Structural, magnetic and electrical properties of Al3+ substituted Ni–Zn ferrite nanoparticles. *Journal of Alloys and Compounds*, *511*(1), 107-114.

[45] Wang, J., Xiang, C., Liu, Q., Pan, Y., & Guo, J. (2008). Ordered mesoporous carbon/fused silica composites. *Advanced Functional Materials*, *18*(19), 2995-3002.

[46]   Colaneri, N. F., & Schacklette, L. W. (1992). EMI shielding measurements of conductive polymer blends. *IEEE transactions on instrumentation and measurement*, *41*(2), 291-297.

[47]   Jana, P. B., Mallick, A. K., & De, S. K. (1992). Effects of sample thickness and fiber aspect ratio on EMI shielding effectiveness of carbon fiber filled polychloroprene composites in the X-band frequency range. *IEEE transactions on electromagnetic compatibility*, *34*(4), 478-481.

[48]   Hong, Y. K., Lee, C. Y., Jeong, C. K., Lee, D. E., Kim, K., & Joo, J. (2003). Method and apparatus to measure electromagnetic interference shielding efficiency and its shielding characteristics in broadband frequency ranges. *Review of scientific instruments*, *74*(2), 1098-1102.

[49]   Bayat, M., Yang, H., Ko, F. K., Michelson, D., & Mei, A. (2014). Electromagnetic interference shielding effectiveness of hybrid multifunctional Fe3O4/carbon nanofiber composite. *Polymer*, *55*(3), 936-943.

[50]   Petrova, E., Kotsikau, D., Pankov, V., & Fahmi, A. (2019). Influence of synthesis methods on structural and magnetic characteristics of Mg–Zn-ferrite nanopowders. *Journal of Magnetism and Magnetic Materials*, *473*, 85-91.

[51]   Muccillo, R., Muccillo, E. N. S., & Kleitz, M. (2012). Densification and enhancement of the grain boundary conductivity of gadolinium-doped barium cerate by ultra fast flash grain welding. *Journal of the European Ceramic Society*, *32*(10), 2311-2316.

[52]   Ayub, S., Guan, B. H., Ahmad, F., Javed, M. F., Mosavi, A., & Felde, I. (2021). Preparation methods for graphene metal and polymer based composites for emi shielding materials: State of the art review of the conventional and machine learning methods. *Metals*, *11*(8), 1164.

[53]   Shakir, M. F., Tariq, A., Rehan, Z. A., Nawab, Y., Abdul Rashid, I., Afzal, A., ... & Muttaqi, M. (2020). Effect of Nickel-spinal-Ferrites on EMI shielding properties of polystyrene/polyaniline blend. *SN Applied Sciences*, *2*, 1-13.